Yueming Liang

Alexander V. Spuskanyuk

Shane E. Flores

Mechanical Engineering Department,
Materials Department,
University of California,
Santa Barbara, CA 93106

David R. Hayhurst
School of Mechanical,
Aerospace and Civil Engineering,
The University of Manchester,
Manchester, M60 1QD, UK

John W. Hutchinson
Division of Engineering
and Applied Sciences,
Harvard University,
Pierce Hall, Cambridge, MA 02138

Robert M. McMeeking

Anthony G. Evans

Mechanical Engineering Department,
Materials Department,
University of California,
Santa Barbara, CA 93106

The Response of Metallic Sandwich Panels to Water Blast

Metallic sandwich panels subject to underwater blast respond in a manner dependent on the relative time scales for core crushing and water cavitation. This article examines the response at impulses representative of an (especially relevant) domain: wherein the water cavitates before the core crushes. Three core topologies (square honeycomb, I-core, and corrugated) have been used to address fundamental issues affecting panel design. Their ranking is based on three performance metrics: the back-face deflection, the tearing susceptibility of the faces, and the loads transmitted to the supports. The results are interpreted by comparing with analytic solutions based on a three-stage response model. In stage I, the wet face acquires its maximum velocity with some water attached. In stage II, the core crushes and all of the constituents (wet and dry face and core) converge onto a common velocity. In stage III, the panel deflects and deforms, dissipating its kinetic energy by plastic bending, stretching, shearing, and indentation. The results provide insight about three aspects of the response. (i) Two inherently different regimes have been elucidated, designated strong (STC) and soft (SOC), differentiated by a stage II/III time scale parameter. The best overall performance has been found for soft-core designs. (ii) The foregoing analytic models are found to underestimate the kinetic energy and, consequently, exaggerate the performance benefits. The discrepancy has been resolved by a more complete model for the fluid/structure interaction. (iii) The kinetic energy acquired at the end of the second stage accounts fully for the plastic dissipation occurring in the third stage, indicating that the additional momentum acquired after the end of the second stage does not affect panel performance. [DOI: 10.1115/1.2178837]

1 Introduction

The response of metallic sandwich panels to the impulse caused by underwater blast has been the subject of several recent assessments [1–7]. The scenario of interest is depicted in Fig. 1. An impulse from the water impinges on a panel rigidly supported around its perimeter. The blast wave causes the core to compress and the panel to deflect. It is desirable to design panels that (for equivalent weight per area) beneficially affect the following three performance metrics, in order of importance:

A. The incidence and extent of dynamic tearing of the front (or wet) face.
B. The center deflection of the back (or dry) face.
C. The load imparted to the supports.

The benchmark is a solid plate of the same material with identical weight per area. The intent is to probe the influence of topology on all three performance metrics and thereby provide insights into the design of optimal panels. In the present paper, numerical simulation is used to ascertain responses that can be expressed in a form amenable to comparison with available analytic solutions.

Results for a plane impulse provide the fundamental perspective [2–7].

The analysis originates with a temporally distinct three-stage model for air blast (Fig. 1) [2–5]. In stage I, the impulse imparts a momentum to the front face which dictates its kinetic energy. In stage II, the front face decelerates as the core and back face accelerate, until a common velocity is attained. At the end of this stage, the momentum and kinetic energy are the same as those experienced by a solid plate having the same mass per area. Finally, in stage III, the kinetic energy is dissipated by plastic bending, stretching, and indentation of the panel.

While the response to water blast may not be temporally separable in such explicit manner (and for certain panels may be inseparable even for air blast), the three stages remain a useful concept. The extension to water blast has been pursued through the incorporation of the fluid/structure interaction (FSI) [4]. This assessment has identified four different domains differentiated by their cavitation and core crushing characteristics. To set the objectives of the present study, the key features of this FSI analysis are described in the following section.

2 Background Analysis

2.1 Initial Response. Consider a panel with total mass per unit area,

$$m_{\text{total}} = m_f + m_b + m_c \tag{1}$$

with m_f the mass per unit area of the front face, m_b that for the back face, and m_c the mass per unit area of the core. The impinging wave has the form [3–5]:
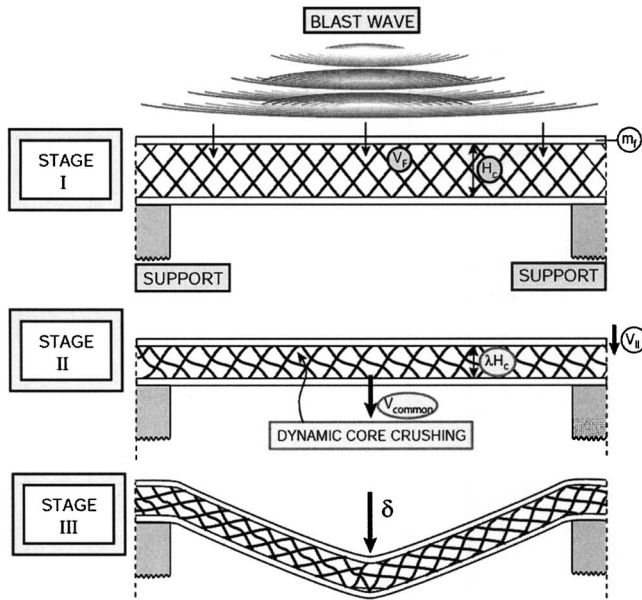
Fig. 1 A schematic showing the three temporally distinct stages that accompany a panel subject to air blast [3]

$$p_I = p_0 e^\xi,$$

$$\xi = \frac{x}{c_w t_0} - \frac{t}{t_0},$$

with t_0 the characteristic decay time for the pulse and t the time after the blast first arrives at the fluid/structure interface (at $x=0$). Thereafter, the pressure in the water is (for $\zeta = x/c_w t_0 + t/t_0 > 0$) [4,5]:

$$p(x,t) = p_0 \left[e^\xi - \left(\frac{2\beta}{1-\beta} + \frac{\sigma_{YD}^c}{p_0} \right) e^{-\beta\zeta} + \frac{1+\beta}{1-\beta} e^{-\zeta} + \frac{\sigma_{YD}^c}{p_0} \right],$$

$$(2a)$$

and (for $\zeta < 0$)

$$p(x,t) = p_0 e^\xi \qquad (2b)$$

with the fluid/structure interaction parameter, $\beta = \rho_w c_w t_0 / m_f$. The corresponding velocity distribution is (for $\zeta > 0$):

$$v(x,t) = \frac{p_0}{\rho_w c_w} \left[e^\xi + \left(\frac{2\beta}{1-\beta} + \frac{\sigma_{YD}^c}{p_0} \right) e^{-\beta\zeta} - \frac{1+\beta}{1-\beta} e^{-\zeta} - \frac{\sigma_{YD}^c}{p_0} \right]$$

$$(3a)$$

and (for $\zeta < 0$)

$$v(x,t) = \frac{p_0}{\rho_w c_w} e^\xi. \qquad (3b)$$

The water begins to cavitate at location $x = x_c$ after time $t = t_c$, when the pressure in the water first satisfies:

$$p(x_c, t_c) = 0 \qquad (4a)$$

and

$$\frac{\partial p(x_c, t_c)}{\partial x} = 0. \qquad (4b)$$

This event coincides with the end of stage I. The fluid pressure and

velocity profiles at the end of this stage are thus obtained from Eqs. (2a) and (3a) as:

$$p'(x) = p(x, t_c)$$
$$v'(x) = v(x, t_c)$$

$$(5)$$

This occurs at time:

$$t_c \approx t_0 (\ln \beta) / (\beta - 1).$$

The pressure and velocity characteristics at this time for $\beta = 3.125$ and $\sigma_{YD}^c / p_0 = 0.18$ are shown in Fig. 2(a), together with finite element calculations elaborated later. Subsequently, a cavitation front moves through the water, away from the panel, exemplified by the pressure and velocity distributions at $t = 2t_c$ plotted in Fig. 2(b).

At this stage, the momentum of the front face and attached water layer (added mass) ($x_c < x < 0$) is:

$$M_F = m_f v_{\text{face}} + \int_{x_c}^0 \rho_w v'(x) dx, \qquad (6)$$

while that acquired by the core plus back face is [5]:

$$M_B = \sigma_{YD}^c t_c. \qquad (7)$$

In the preceding formulas, σ_{YD}^c is the "dynamic strength" of the core and is assumed constant in time. It is the stress induced in the core, immediately adjacent to the front face, at the onset of cavitation. For a material with linear hardening, tangent modulus, E_T (typical for stainless steels), the following approximate form has been proposed [8]:

$$\frac{\sigma_{YD}^c}{\sigma_Y \bar{\rho}} \equiv \lambda_D \approx 1 + \sqrt{\frac{E_T}{E}} \left(\frac{v_{\text{face}}}{c_{el} \varepsilon_Y} - 1 \right). \qquad (8)$$

Here $c_{el} = \sqrt{E/\rho}$ is the relevant elastic wave speed in the constituent material, σ_Y is its yield strength, and ε_Y is its yield strain (at the relevant strain-rate). To determine σ_{YD}^c from (8), the front face velocity, v_{face}, must be determined from (3a) at $x=0$, $t=t_c$, leading to an implicit expression. As an alternative, the velocity can be estimated from (3a) with the core yield strength set to zero; the result is almost the same. It will be shown below that (8) provides a reasonably accurate measure of σ_{YD}^c for each of the cores examined in this investigation.

The pressure pulses caused by underwater explosions are more complex. The growth and collapse of bubbles caused by the expansion and compression of the explosion gases, as well as the interaction of the buoyant bubble and its acoustic signals with the sea bottom, the water surface, and the structure [9–12], lead to pressure waves having complicated forms. Nevertheless, the initial pressure rise and its decay at locations below the surface are well characterized by the preceding forms. Most of the differences between the present model and the reality of an underwater explosion occur after the initial pressure rise has decayed to moderate levels [9–12]. The secondary pressure spikes that arrive later do not cause significant damage to a well-designed structure that has survived the initial impulse, as described later. So we focus on the initial pressure wave and its effect on the structures of interest. It is also true that the simple exponential decay after the sharp spike of pressure is an idealization, with some oscillation of the pressure occurring superposed on the exponential form [9]. However, these pressure oscillations are minor and do not significantly alter the effect of the impulse on the deforming structure.

2.2 Impulsive Domains. The response of the panel in stage II depends on the magnitudes of the impulse, the FSI parameter, β, and the mass [4]. Key aspects have been elucidated by envisaging homogenized cores at appropriate relative densities [4]. Four domains emerge, illustrated using two additional parameters: a nondimensional impulse [4],
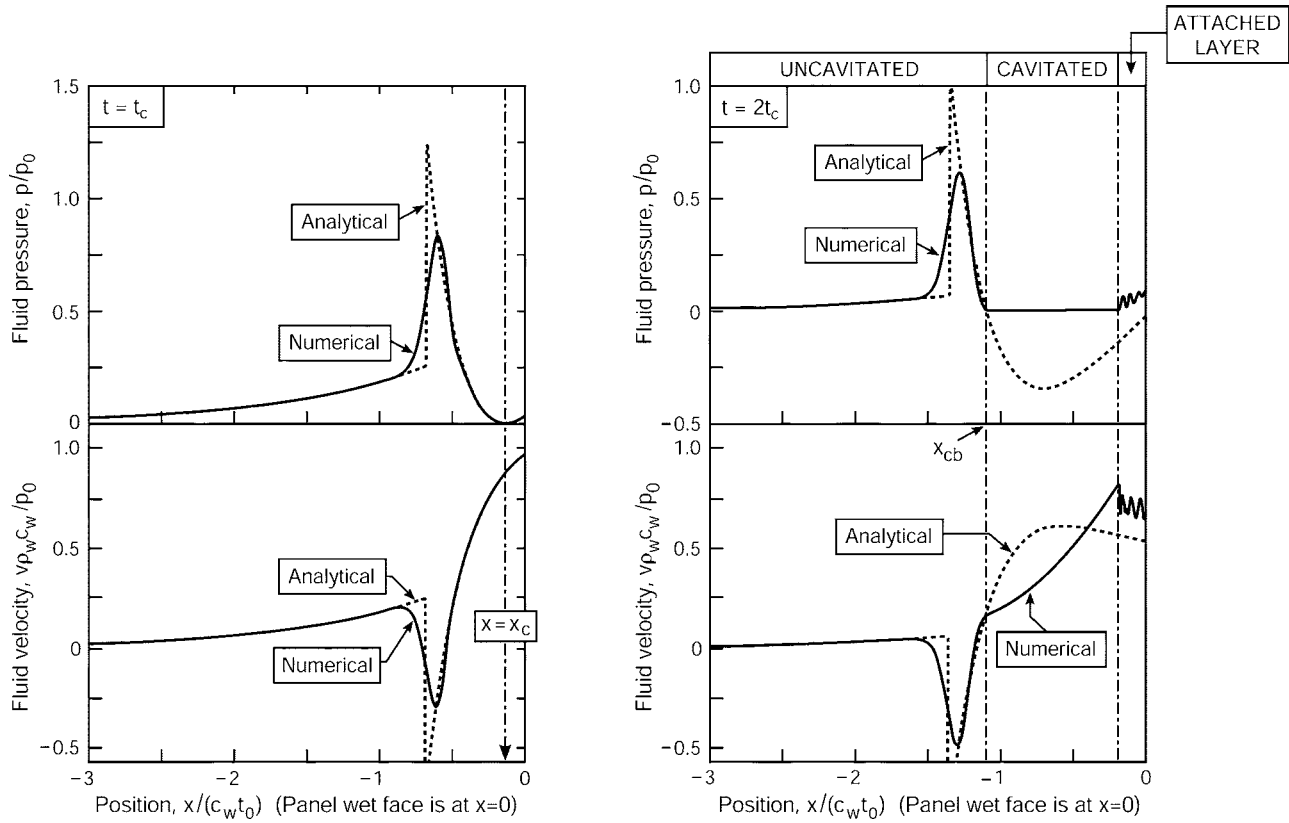
Fig. 2 The trends in pressure and velocity in the water at times t_c and $2t_c$ (with t_c designating the instant when cavitation commences). The plots compare the analytic solution with a calculation conducted using ABAQUS/Explicit. After t_c, cavitation fronts propagate through the water (towards and away from the panel) leaving a zone of cavitated water in their wakes. Note that, at the cavitation front, the water has positive velocity in the direction of motion of the panel. The equivalent thickness of the sandwich panel is 20 mm. The core has a relative density of 0.03 and yield strength of $\sigma_{YD}^c/p_0=0.18$. The thickness of the front face is 6 mm so that $\beta=3.125$ and that of the back face is 8 mm.

$$\bar{I} = \frac{2I_o t_o}{m_f H_c} \tag{9a}$$

and a nondimensional mass,

$$\bar{m} = \frac{m_c}{m_f}, \tag{9b}$$

where H_c is the core height. The domains are illustrated on Fig. 3 [4] for levels of impulse and panel dimensions representative of those to be explored in the present study ($\bar{I} \approx 0.5, \bar{m} \approx 1$). They comprise a high strength domain (IV) in which the core is completely resistant to crushing and a low strength, small β, domain (I) in which the core completely crushes before the water cavitates. Two intermediate domains (II and III), in which the cores partially crush, are especially relevant. In domain II, *cavitation occurs in the water* (at location $x_c < 0$) before core crushing is complete. Domain III also involves partial crushing, but differs in the sense that cavitation occurs at the front face ($x_c = 0$), not in the water. It arises when the cores are stronger. Contours of transmitted impulse (Fig. 3) indicate how the domains affect the response. Because of its importance to ongoing investigations of blast resistant panels [1–7], *the present study has been designed to probe domain II for representative core topologies.* That is, all of the impulse levels and core topologies result in domain II responses. Subsequent investigations will examine other domains as well as transitions between domains.

2.3 Analytic Formulas for Domain II. Analysis conducted for impulses and cores representative of domain II [5] have provided formulas that benchmark the ensuing numerical results. For-

mulas are available for a design with front and back faces having the same mass [5] expressing the transmitted impulse, I_T, as well as the momentum acquired by the front face, M_F, both inclusive of the mass of attached water between the initial cavitation plane and the structure, and the momentum induced in the core plus back face, M_B. This attached water mass is [5]:

$$m_w = 0.71 m_f \beta \frac{\sigma_{YD}^c}{p_0}. \tag{10}$$

such that

$$\frac{I_T}{I_0} \equiv F_T = 2f + 1.27(1-f)\frac{\sigma_{YD}^c}{p_0} \tag{11a}$$

$$\frac{M_B}{I_0} \equiv F_B = 3.64f\frac{\sigma_{YD}^c}{p_0} \tag{11b}$$

$$M_F \equiv I_0 F_F = I_T - M_B \tag{11c}$$

with $f = \beta^{\beta/(1-\beta)}$.

The kinetic energies acquired by the panel can be determined from these momenta. Inclusive of the mass of the attached water, the KE at the end of stage I, before the core begins to crush, is [5];

$$\mathrm{KE}_I = \frac{M_F^2}{2(m_f + m_w)} + \frac{M_B^2}{2(m_b + m_c)} \tag{12a}$$

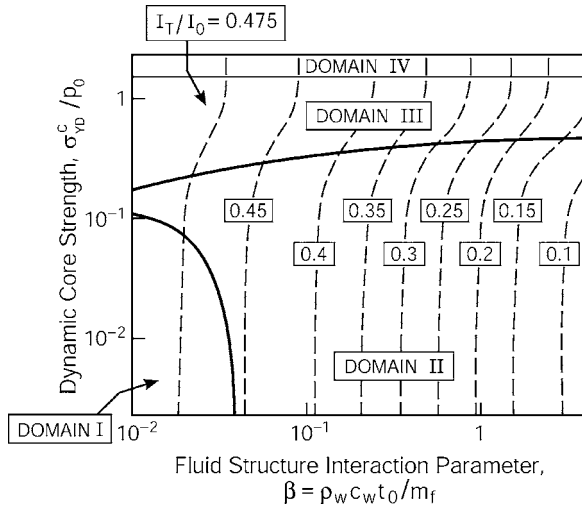and, after stage II, when core crushing is complete [5]:

Fig. 3 Fluid structure interaction map ($\bar{I}=0.5$, $\bar{m}=1.0$) with axes of core dynamic strength and the Taylor fluid structure interaction parameter β. The four impulse domains are marked on the map. Contours of the impulse transmitted into the sandwich plate at first cavitation are also included [4].

$$KE_{II} = \frac{I_T^2}{2(m_f + m_b + m_c + m_w)}. \quad (12b)$$

In some of the following numerical assessments, the kinetic energies in the structure only (that is, excluding the attached water) are also determined: these are designated KE_I^* and KE_{II}^*.

The times associated with these stages are [5]:

$$t_I = t_c \approx t_0(\ln \beta)/(\beta - 1),$$

$$t_{II} \approx \frac{I_T}{2\sigma_{YD}^c}, \quad (13)$$

$$t_{III} \approx L\sqrt{\rho/\sigma_Y}.$$

At the end of stage II, when temporally distinct from stage III, all constituents attain a common velocity,

$$v_{common} = \sqrt{\frac{2KE_{II}}{m_{total} + m_w}}. \quad (14)$$

During stage II, the crushing strain ε_c of the core is dictated by its ability to absorb the kinetic energy differential, $KE_I - KE_{II}$, through plastic dissipation in the core:

$$W_c \approx \sigma_{YD}^c \varepsilon_c H_c. \quad (15)$$

Equating W_c to $KE_I - KE_{II}$ leads to an expression for the crushing strain [5].

The back face deflection is dictated by the ability of the sandwich to absorb KE_{II}, during stage III. The dissipation involves plastic bending, stretching, shearing, and indentation, subject to the prior core crushing in stage II. When bending and stretching predominate (no shear resistance in the core and no indentation), the dissipation for a panel with both faces having equal thickness rigidly supported at the ends is given by [5]:

$$W_{pl}^{total} = \frac{2}{3}\sigma_Y h_f (2 + \lambda_s m_c/m_f) \left(\frac{\delta_b}{L}\right)^2 + 4\sigma_Y h_f \frac{H_c(1 - \varepsilon_c)}{L} \frac{\delta_b}{L} \quad (16)$$

where $\lambda_s = \sigma_s/\sigma_Y \bar{\rho}$ is a measure of the stretch resistance of the core, with σ_s the stretch strength. The results for other support conditions will be discussed elsewhere [13].
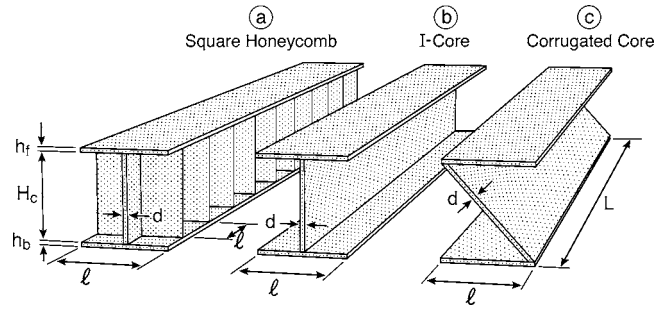

Fig. 4 The geometries of the three core topologies used in the analysis

2.4 Strong and Soft Cores. The possibility that two regimes exist has already been postulated [4]. These regimes emerge vividly in the present study. Their relative incidence is anticipated by the relative time scales for stages II and III expressed by the ratio [14]:

$$\Pi \equiv \frac{t_{II}}{t_{III}} \approx \frac{2I_T}{L\sigma_{YD}^c}\sqrt{\frac{\sigma_Y}{\rho}}. \quad (17)$$

The differing responses are differentiated by a critical value, Π_{th}. When $\Pi < \Pi_{th}$, stages II and III are temporally distinct, enabling the panels to attain a common velocity at the end of stage II, whereupon the response can be analyzed with modifications to the preceding analytical formulas. Panels that respond in this manner are designated *strong core designs* (STC), because high core strength contributes to the sign of the Π inequality. Note that the distance between the supports also affects the transition, so that the STC designation should not be construed to be solely governed by the dynamic strength of the core.

When $\Pi > \Pi_{th}$, stages II and III merge, causing a change in regime. The alternative response is conceptually closer to the buffer plate/crushable core concept [15], with no common velocity. Panels having this response are designated *soft core designs* (SOC), with the caviat that, again, the support length is also involved. It will be demonstrated that, for all three performance-governing metrics (A, B and C, above), SOC designs are preferable. Estimates of Π_{th} will be provided.

3 Scope of the Calculations

Three different core topologies have been selected, based on their geometric versatility and the range in their dynamic strength (Fig. 4). When the core height H_c is significant relative to the span of the panel, it can be considered to represent a double hull system in naval architecture. However, we do not consider our concepts to be restricted to either single or double hull systems, but applicable as appropriate to both possibilities.

 i. A high strength orthotropic core based on the square honeycomb (Fig. 4(*a*)). In the double hull setting, this architecture is known as orthogonally stiffened.
 ii. An I-core with axial characteristics comparable to the honeycomb, but entirely different transverse properties, rendering it amenable to a comprehensive parameter study (Fig. 4(*b*)). In the double hull case, this design is known as unidirectionally-stiffened.
 iii. A corrugated core amenable to a wide sensitivity assessment, upon varying the included angle and the relative density (Fig. 4(*c*)). This design is reminiscent of the Navtruss. However, our architecture differs both in detail and in parametric range.

All calculations are performed without initial imperfections. The role of imperfections, which can be substantial, will be examined in a separate study [13].
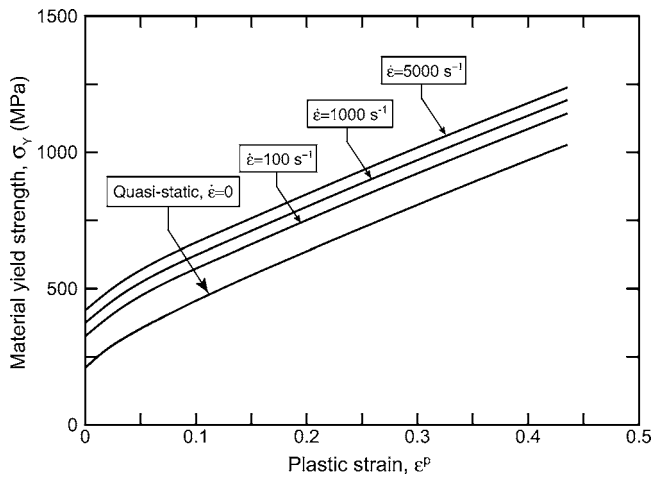
Fig. 5 Dynamic stress/strain curves for 304 stainless steel used in the simulations [8]

Fig. 6 A schematic of the numerical model used in ABAQUS/Explicit

Two different boundary conditions have been pursued.

Condition I. The two faces and the core are rigidly held at the supports. This condition has been used in most prior investigations [1–3,5–7].

Condition II. Only the back face is fixed at two outer supports. Periodic boundary conditions are imposed on the front face, but, otherwise, this face is free to displace into the core and toward the supports.

Note that the applicability of the analytic results (above) is unaffected by the choice of boundary condition through stage II. Differences arise in stage III.

A preliminary numerical assessment, used to refine the scope of the investigation, has revealed the following two characteristics.

    a.   The back face displacements attained for condition I are less than those for condition II. The difference is associated with the diminished front face stretching occurring for the latter.

    b.   The plastic strains in the front face are lower for condition II.

Given the apparently greater importance of tearing than deflection, *condition II has been chosen for most of the ensuing analysis.*

All calculations are performed using a representative free field impulse with pressure/time characteristics ($p_0 = 100$ MPa, $t_0 = 0.1$ ms) indicative of domain II. The consequences of larger impulses and the occurrence of different domains (Fig. 3) will be elaborated in future assessments. The calculations are carried out for panels consisting of 304 stainless steel having the approximately bilinear stress-strain curves depicted on Fig. 5, with appreciable strain-rate sensitivity. All properties and constitutive law details are as summarized in [8]. In addition to calculations for edge-supported beams, some simulations have been carried out for freestanding panels in the form depicted in the side view of Fig. 6 (i.e., without kinematic constraint parallel to the direction of the impulse). These simulations provide results of the type shown as "numerical" on Fig. 2.

The ensuing sections of this article are organized in the following manner. In Sec. 4, the core topologies to be used are geometrically specified. In Sec. 5, the numerical scheme is described and some calibration results presented. Thereafter, in Sec. 6, mechanism identification is used to provide criteria that distinguish STC and SOC responses, emphasizing the different performance metrics in the two domains. In Sec. 7, an alternative analytical model is used to provide a consistent reinterpretation. In Sec. 8, the deflections and the plastic strains in the faces are examined and related to analytic results.
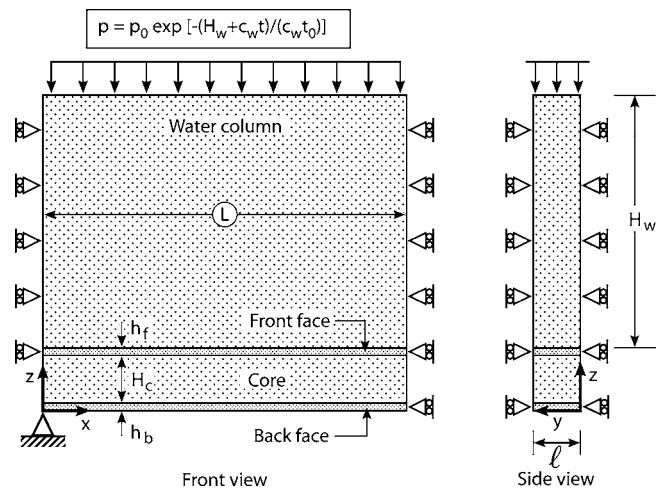
4 Geometries

All panels have fixed mass per unit area, $m_{total} = 160$ kg/m^2, corresponding to a solid plate thickness, $H_{eq} = 2$ cm. The half span is taken to be representative, $L = 1$ m, width $l = 0.1$ m, with the constraint that the core thickness, $H_c/L < 0.4$. The three core topologies (Fig. 4) allow a wide range of geometric options for fixed m_{total}.

For the *square honeycomb*, the benchmark is a core with relative density, $\bar{\rho} = 0.03$, and faces with equal mass, subject to a fixed spacing between core members, $l = 0.1$ m. Around this benchmark design, the core relative density is allowed to vary between $0.01 \leq \bar{\rho} \leq 0.04$ while the spacing, l, is fixed. This is achieved by adding/subtracting mass to the faces in order to retain m_{total}. The ratio of the back to front face thickness, $\Delta = h_b/h_f$, is also varied between 1 and 6 for each $\bar{\rho}$. The latter is used to highlight the influence of the faces on the fluid/structure interaction.

The *I-core* density was varied between $0.01 \leq \bar{\rho} \leq 0.06$, with particular emphasis on relative core height in the range, $0.1 \leq H_c/L \leq 0.3$. The face thickness ratio Δ was varied between 1 and 7, again achieved by redistributing the mass between the faces and the core to maintain m_{total}. Two specific geometries provide the clearest distinction between strong and soft responses. The STC response is illustrated by a system having dimensions h_f
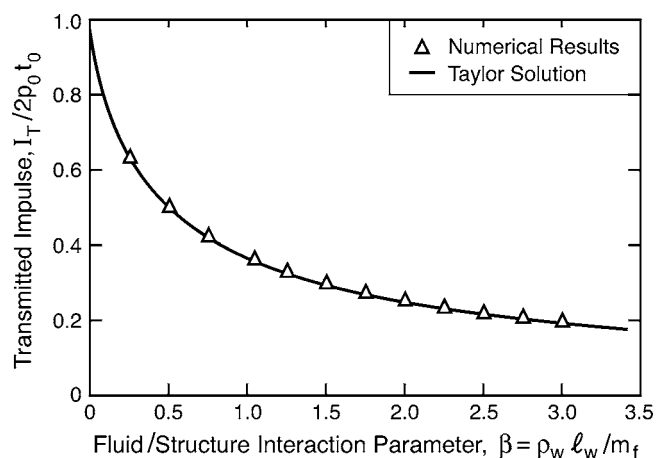

Fig. 7 The predictions of the transmitted impulse conducted for a solid plate using ABAQUS/Explicit and the comparison with the analytic solution given by Taylor [17]
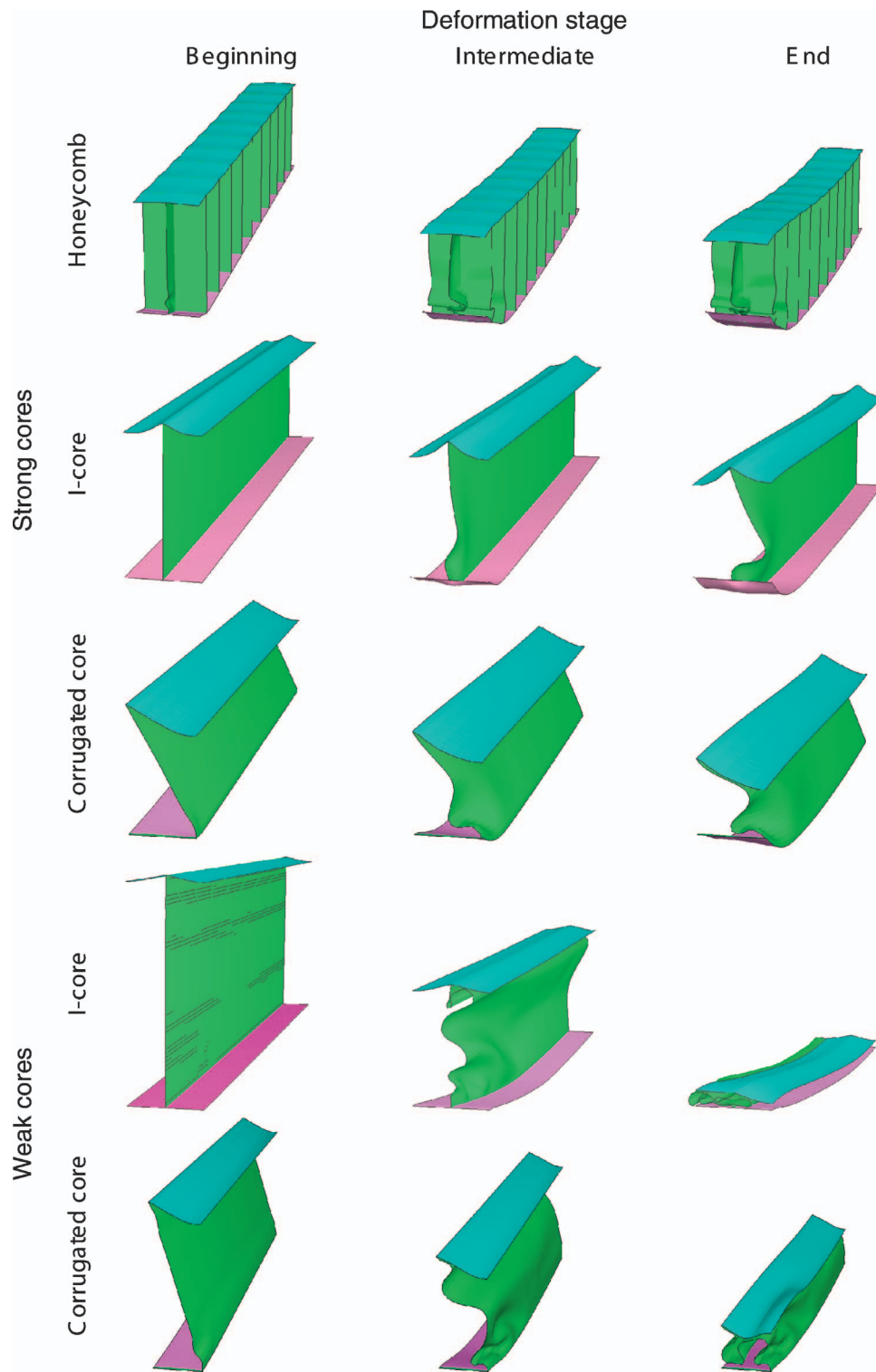
Fig. 8 The deformations predicted using the numerical model for the three cores shown in Fig. 4. Results for the I-cores and the corrugated cores are shown for both strong and soft responses.

$=2$ mm, $h_b=6$ mm, $H_c=20$ cm, and $\bar{\rho}=0.06$. The SOC response is demonstrated using dimensions: $h_f=4$ mm, $h_b=12$ mm, $H_c=30$ cm, and $\bar{\rho}=0.013$.

For the *corrugated core*, the relative densities were in the range $0.01 \leqslant \bar{\rho} \leqslant 0.05$. The height of the core was varied within $0.05 \leqslant H_c/L \leqslant 0.4$ by changing the angle, θ. The face thickness ratio Δ was allowed to vary subject to the constraint, $h_f \geqslant 2$ mm. Again,

two geometries are used to distinguish the responses. The SOC response is demonstrated using the dimensions, $\bar{\rho}=0.02$, $\Delta=5.5$, and $H_c/L=0.3$. The STC response is found using dimensions $\bar{\rho}=0.05$, $\Delta=4$, and $H_c/L=0.2$.

Given that the I-cores and the corrugations are anisotropic, choices must be made regarding the orientation. The present assessment is conducted in the "stronger" orientation. That is, for
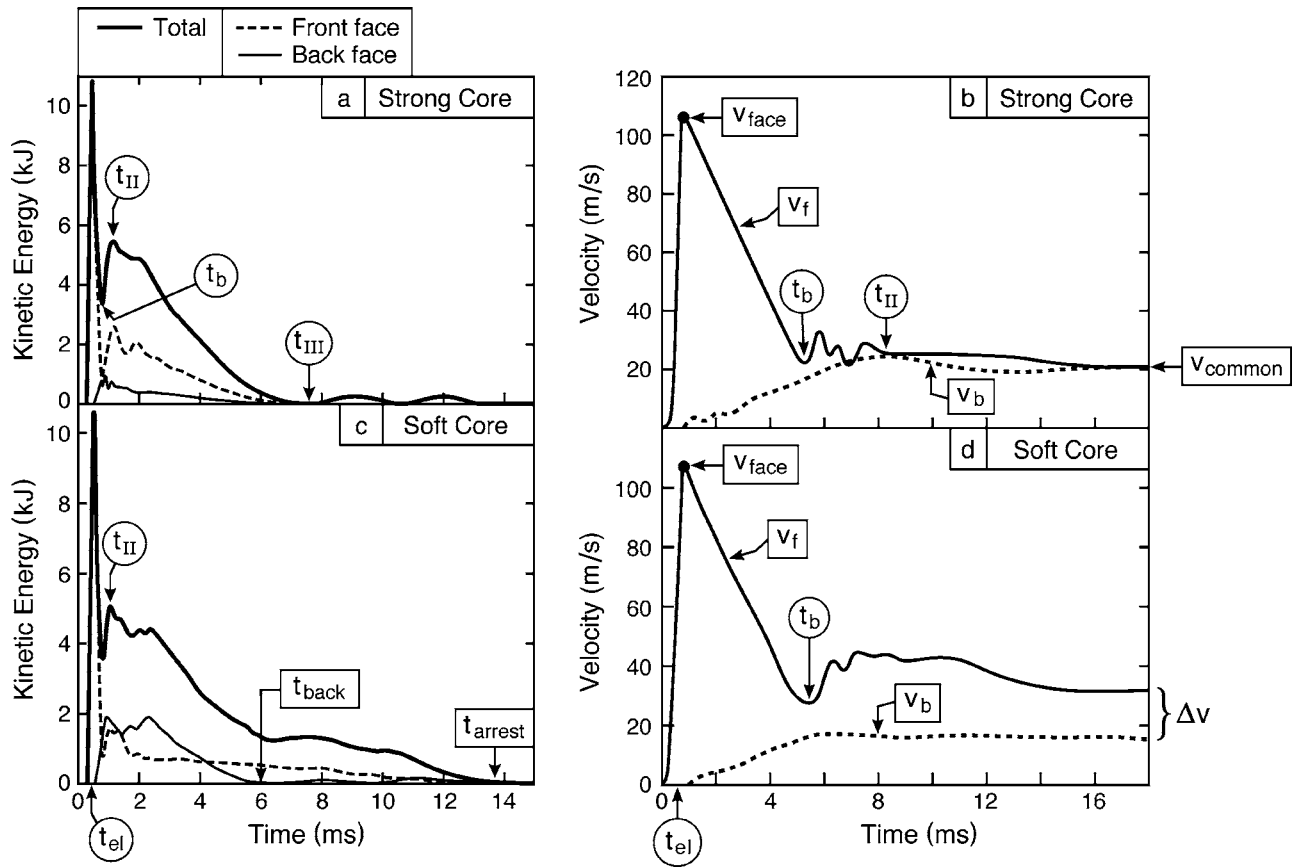
Fig. 9 The constituent velocities and kinetic energies obtained for corrugated cores: (*a*) and (*b*) refer to a strong core with relative density, $\bar{\rho}=0.05$, $\Delta=4$, and $\beta=9.375$ while (*c*) and (*d*) refer to a soft core with $\bar{\rho}=0.02$, $\Delta=5.5$, and $\beta=8.70$.

the I-and corrugated cores, the members are axial and continuous between the supports (Fig. 4). This orientation is orthogonal to that analyzed by Rabczuk et al. [7], who studied panels having the core members aligned transversely. With all other parameters held fixed, the differing orientations generate very different trends, as discussed later. The rationale for the present choice has been motivated by 3-D simulations (Appendix A), which suggest that the dynamic responses of square panels are largely governed by the behavior along the "strong" direction. Future assessments will elaborate and clarify the role of anisotropy.

5 The Numerical Scheme and Calibration Tests

The numerical model (Fig. 6) consists of a water column above the sandwich panel. Contact is enforced at the interface between the water and the panel. Symmetry boundary conditions are applied at all surfaces, except at the back face support (at $x=0$), which is clamped. A uniform pressure boundary condition is imposed on the top surface of the water column. Numerical tests have ascertained that, to correctly capture the fluid/structure interactions, the height of the column must satisfy: $H_w \geq 4H_c$.

The commercial code, ABAQUS/Explicit [16], is used. Eight-node 3D brick elements with reduced integration (C3D8R) are employed to model the water, while four-node shell elements (S4R), with five integration points through the thickness, are used to model the faceplates and the core members. The water is assumed to be linear elastic under compression, with zero tensile strength and zero shear modulus. (Some simulations have been performed with a small finite shear modulus, $G/c_w^2\rho_w=10^{-6}$, to affirm that the results are negligibly different from those with zero shear modulus). Thus, the pressure (p) in the water is given by:

$$p = -c_w^2\rho_w\varepsilon_V, \ (\varepsilon_V < 0)$$

$$p = 0, \ (\varepsilon_V < 0)$$

(18)

where $\varepsilon_V=\int_0^t(\partial v_i/\partial x_i)dt$ is the fluid volume strain. Thus when $\varepsilon_V \geq 0$, all stresses in the water become zero, causing cavitation.

Careful consideration has been given to the artificial bulk viscosity coefficients. The default coefficients designated in ABAQUS/Explicit give excessive dissipation in the water that diminishes the pressure before the impulse reaches the structure. Consequently, the coefficients have been systematically reduced until the blast wave pressure closely matches p_0 when it confronts the panel. The values utilized are $b_1=0.02$ and $b_2=0.2$ [16]. To affirm the fidelity of the approach, numerical results for a free-standing metal plate have been obtained and compared with the analytic solution given by Taylor [17] (Fig. 7).

For each simulation, the following parameters are obtained:

i. The final mid-point deflections of the faces: front, δ_f, and back, δ_b.

ii. The core crushing strain, ε_c.

iii. The velocities of the faces (front, v_f and back, v_b) as a function of time, t, after the impulse contacts the front face.

iv. The kinetic energies of the two faces (KE_{front} and KE_{back}) and the core (KE_{core}) and the total (KE_{total}), as a function of time.

v. The plastic dissipation, $W_{pl}^{constituent}$, in each constituent as a function of time.

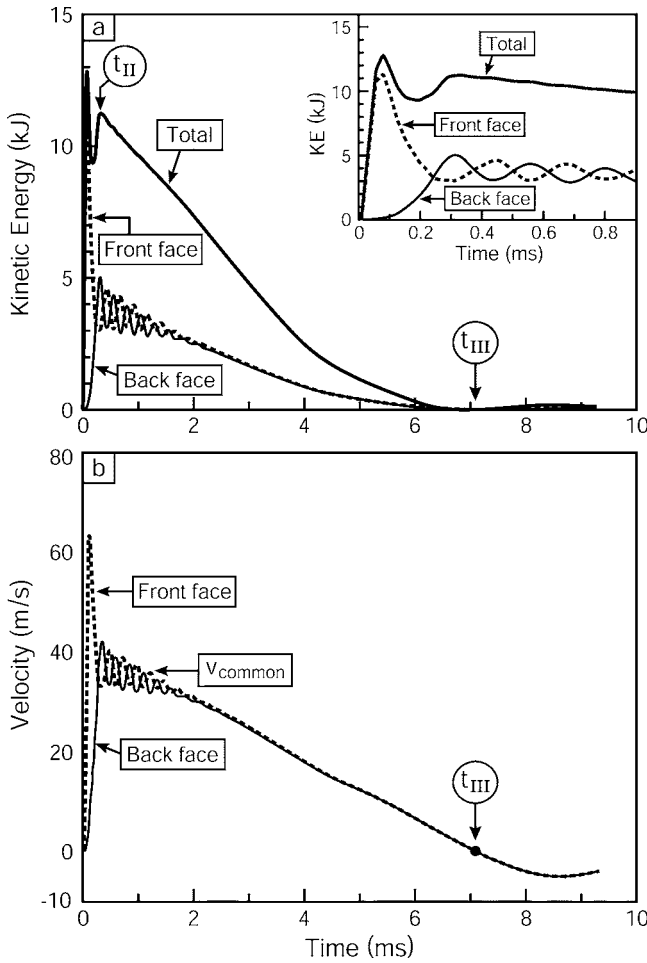vi. The reaction forces, P_{react}, at the supports as a function of time.

Fig. 10 The kinetic energies and velocities for a square honeycomb core with $\bar{\rho}=0.03$, $\Delta=1$, and $\beta=2.68$
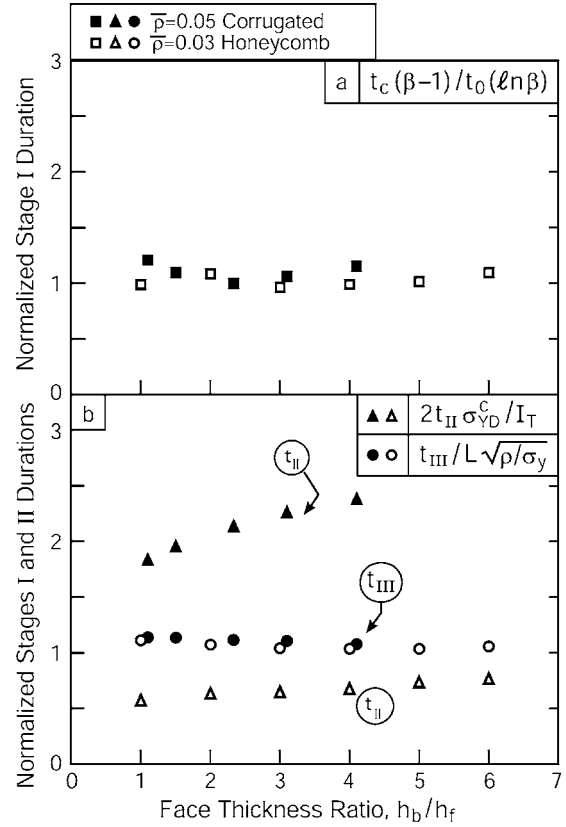

Fig. 11 The durations of stages I, II, and III normalized by the expressions derived using the analytic model (Sec. 1): $t_c/t_0\ln\beta/(1-\beta)$, $t_{II}/(I_T/2\sigma_{YD}^c)$, and $t_{III}/L\sqrt{\rho/\sigma_Y}$

vii. The largest plastic strain, $\varepsilon_{pl}^{\max}$, in the two faces.

The reaction force, P_{react}, is taken as the summation of all nodal forces on the clamped edge of the back face.

At any instant, the average speed, v_i, of element i is obtained through finite element interpolation, once the velocities of its nodes have been ascertained. Then its kinetic energy is obtained ($\text{KE}_i=(1/2)m_iv_i^2$, with m_i the mass of the element) and the total kinetic energy of the constituent determined from the summation:

$$\text{KE}_{\text{constituent}} = \sum_{i=1,n_E} \text{KE}_i, \tag{19a}$$

where n_E is the number of elements in the constituent. The total kinetic energy in the structure is ascertained as:

$$\text{KE}^* = \text{KE}_{\text{front}} + \text{KE}_{\text{back}} + \text{KE}_{\text{core}} \tag{19b}$$

The kinetic energy in the attached water at the end of stage II is also evaluated for STC designs. For this purpose, the average velocity of the panel, v_{common}, at the end of stage II is first obtained. Then, by monitoring the fluid velocity at various locations near the wet surface, the thickness, $|x_a|$, of the attached layer adjacent to the panel (namely the thickness of the fluid having the same velocity) is determined. The kinetic energy of the attached layer is then $\text{KE}_{\text{water}}=lL\rho_w|x_a|v_{\text{common}}^2/2$.

The plastic dissipation in each element is calculated using:

$$W_{pl}^i = \Delta V \int_0^{\varepsilon_p} \sigma_Y d\varepsilon_p, \tag{20}$$

with ε_p the effective plastic strain and ΔV the volume of the element. Thereafter, the total plastic dissipation in each constituent is given by the summation,

$$W_{pl}^{\text{constituent}} = \sum_{i=1,n_E} W_{pl}^i. \tag{21}$$

In ABAQUS, such summations are performed automatically.

Since the bending deflections of the panel are negligible in stages I and II, the velocities can be ascertained from the associated kinetic energies: $v_f=\sqrt{2\text{KE}_{\text{front}}/m_f}$ and $v_b=\sqrt{2\text{KE}_{\text{back}}/m_b}$.

6 Mechanism Identification

General Features. Many different calculations have been used to probe the response space. Only the distinctive results are presented. The displacement sequences (Fig. 8) affirm that two inherently different (STC and SOC) responses exist. The most obvious distinction is that the soft cores collapse during stage III. For the range of topologies examined, honeycomb cores are always STC, while cores with I- and corrugated topologies exhibit both responses, dependent on geometry. The major distinction between the two domains can be ascertained from typical plots of the velocities and kinetic energies (Figs. 9 and 10) of the constituents. To be complementary, and to reveal aspects of the response over different time domains, the KE results in Fig. 9 are presented over the entire structural response time, while the velocity results are confined to shorter times (of order t_{II}). For clarity of presentation, the KE plots for the core have been excluded (since they can be readily inferred from the total KE and the KE for the two faces).

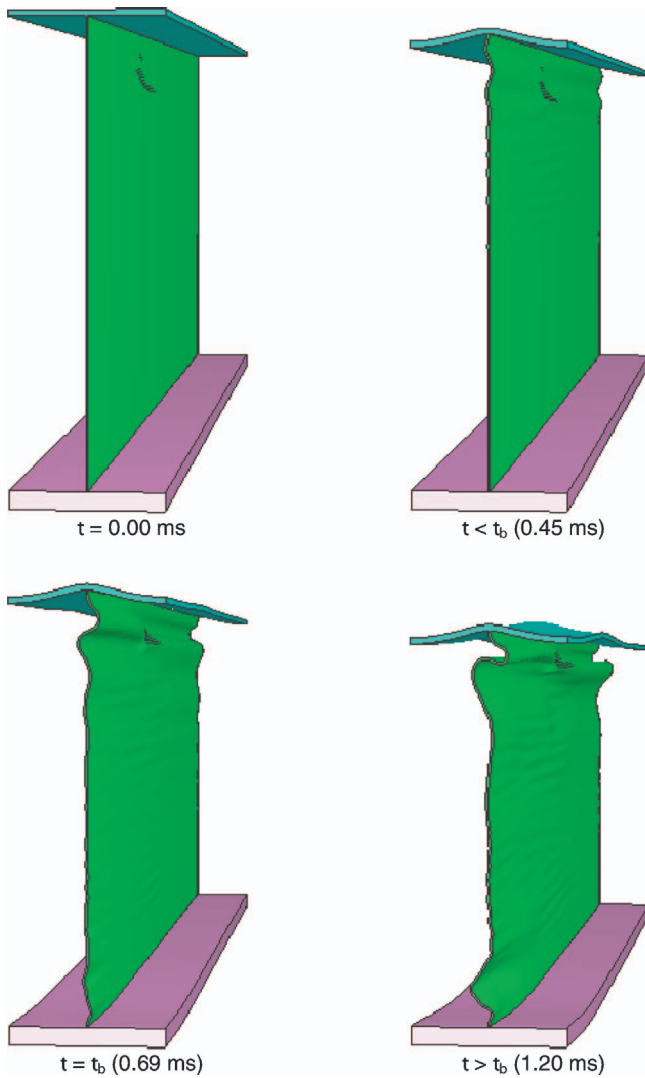*Strong Cores.* In *all STC designs*, exemplified by the corrugated

Fig. 12 A deformation sequence for a soft I-core showing the dynamic elastic buckling of the core near the back face at instant t_b (H_c=0.3L, $\bar{\rho}$=0.013, Δ=3, and β=4.69).

core with $\bar{\rho}$=0.05, Δ=4, and β=9.375 (Figs 9(a) and 9(b)) and the honeycomb with $\bar{\rho}$=0.03, Δ=1, and β=2.68 (Fig. 10), the total kinetic energy in the structure, KE_{II}^*, exhibits two peaks. The first is coincident with time t_c. The second coincides with the end of stage II, t_{II}, when all constituents have attained a common velocity, v_{common}, apparent from plots of the front and back face velocities (Figs. 9 and 10). Note that, for some strong cores, the front face acceleration stops *before the end of stage II*, at time $t_b < t_{II}$ (Fig. 9). Conversely, the back face continues to accelerate up to t_{II}, before attaining v_{common}. The significance of t_b will become apparent later. In stage III, the KE's and velocities of all constituents decrease as energy is dissipated by plastic deformation of the faces and the core. *They reach zero simultaneously in all constituents*. This occurs at time t_{III}, coincident with the back face reaching its final, permanent deflection (Figs. 9 and 10). Some differences among core topologies are apparent at durations close to t_{II} (cf. Figs. 9 and 10). Namely, the square honeycomb and I-cores exhibit distinctive elastic oscillations, duration t_{el}, as the two faces settle into a common velocity (Fig. 10). Similar oscillations have been reported by Deshpande and Fleck [4]. Conversely, the oscillations found for the strong corrugated cores are less distinctive (Fig. 9) and the two faces approach the common velocity differently. The importance of this distinction will become apparent

later. The durations of the stages (Fig. 11) merit comment. Those for stage I, t_c/t_0 ln $\beta/(1-\beta)$, and stage III, $t_{III}/L\sqrt{\rho/\sigma_Y}$, are the same for all strong cores and completely consistent with the analytic models (Eqs. (13)). However, $t_{II}/(I_T/2\sigma_{YD}^c)$ not only differs from the analytic model, but also has different values for honeycomb and corrugated cores. The implications will become apparent later.

Soft Cores. In *SOC designs*, exemplified by a corrugated core with $\bar{\rho}$=0.02, Δ=5.5, and β=8.70 (Figs. 9(c) and 9(d)), there are marked differences in the kinetic energies and velocities from the STC examples. While KE_{back} still approaches zero at time $t \approx t_{III}$, *the front face and the core continue to move and their kinetic energies only become zero at longer times*, $t \approx t_{\text{arrest}} \approx 2t_{III}$. However, beyond t_{III} the back face is elastic and dissipation occurs only due to core and front face plasticity. The temporal pattern of velocities also differs. Most notable, the accelerations of the faces stop at time, $t \approx t_b < t_{II}$ (Fig. 9(d)). One consequence is that the velocity acquired by the back face is smaller than that found in comparable strong cores. Additionally, between t_b and t_{II}, the front face velocity *increases*. The implication is that the soft response is coincident with events occurring at time t_b. An investigation of the phenomena occurring in soft I-cores with $\bar{\rho}$=0.013, Δ=3, and β =4.69 (Fig. 12) reveals that, *exactly at t_b* (0.55 ms in this case), the core buckles at the intersection with the back face.

Displacements. The back face displacements are distinctive (Fig. 13), visualized using displacement surfaces with the following coordinates: core density, $\bar{\rho}$, and relative thickness, Δ. *For all strong cores, δ_b is lowest at large $\bar{\rho}$. Conversely, for all soft cores, δ_b is lowest for small $\bar{\rho}$*. All cores result in smaller displacements at larger Δ.

Plastic Strains. Preliminary assessment of the face tearing susceptibility uses the plastic strain as a metric. A more complete ranking awaits incorporation of a dynamic failure criterion into the FE code. The premise is that *the largest equivalent plastic strain in the faces*, at any lengthwise location, averaged over the width, l, provides the relevant scaling. (Tearing of the core is regarded as relatively benign.) A series of plastic strain results is presented in Fig. 14. Several features emerge.

a.   The strains in the front face are considerably lower than those found in the equivalent impulsive loading of the same panels subject to support condition I (results not shown).

b.   For the front face, in all cases (that is, for both STC and SOC), the strains are lowest for panels having similar front and back face thickness, $\Delta \approx 1$, and cores with lowest relative density, $\bar{\rho} \approx 0.01$. Consequently, there is a conflict with designs based on deflection (Fig. 13). *The conflict is least for soft cores, which demonstrate benefit in both tearing and deflection at low relative density*. The remaining conflict is in front face thickness, because for thin faces, relatively large plastic strains arise due to bulging between core members (Fig. 8). A compromise will be required.

c.   The strains in the back face are invariably larger than at the front, especially in the vicinity of the supports. But again, the SOC designs result in smaller strains.

Force and Impulses. The reaction forces at the supports reveal corresponding features (Fig. 15(a)). The strong cores generate relatively large forces over duration t_{III}. *During the same interlude, the soft cores impart lower forces*. However, for SOC designs the forces persist to longer times, $t > t_{III} \approx 6$ ms, and may become larger after t_{III}. Trends in the peak force with core design, plotted in Fig. 16, demonstrate the specific benefits of soft cores. A further assessment of reaction forces will be described elsewhere [13]. The integral of the forces over time provides the total transmitted impulse, I_{total} (Fig. 15(b)). This measure of the impulse is found to be approximately the same as the free field
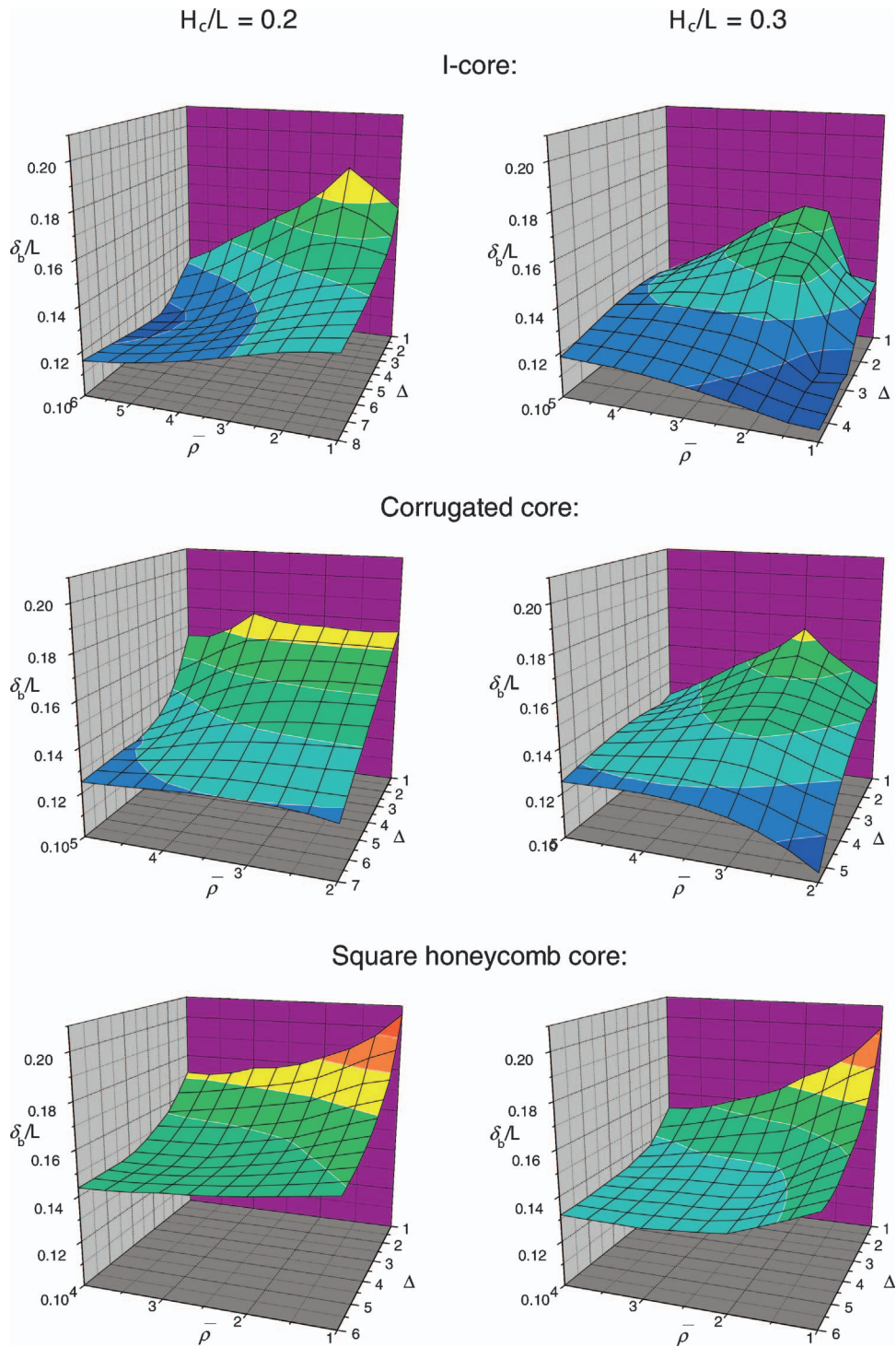
Fig. 13   A synopsis of back face displacement ascertained for a wide range of strong and soft cores. The coordinates are the ratio of back to front face thickness, Δ, and the relative density of the cores, $\bar{\rho}$.

momentum $I_0 = p_0 t_0$ in all cases. As noted earlier, the back face is elastic for $t > t_{III}$, indicating that the impulse beyond t_{III} does not make a significant contribution to the permanent deformation of the panel. The momentum acquired by the structure, plus the attached water, at the end of stage II is more pertinent to the goals of the present assessment. It is the analog of I_T, specified by the analytic model (11a), which dictates KE_{II}. The momentum determined numerically will be given a separate designation, M_T.

Trends in M_T and I_{total} are summarized in Fig. 17 for a range of core designs.

To compare these results with those predicted by the analytic model, the dynamic strength of the core, σ_{YD}^c, must be ascertained. A detailed assessment has found that, *for the present designs*, (8) *provides acceptable fidelity* upon incorporating the front face velocity ascertained at t_c from the modified Taylor formula (3a).
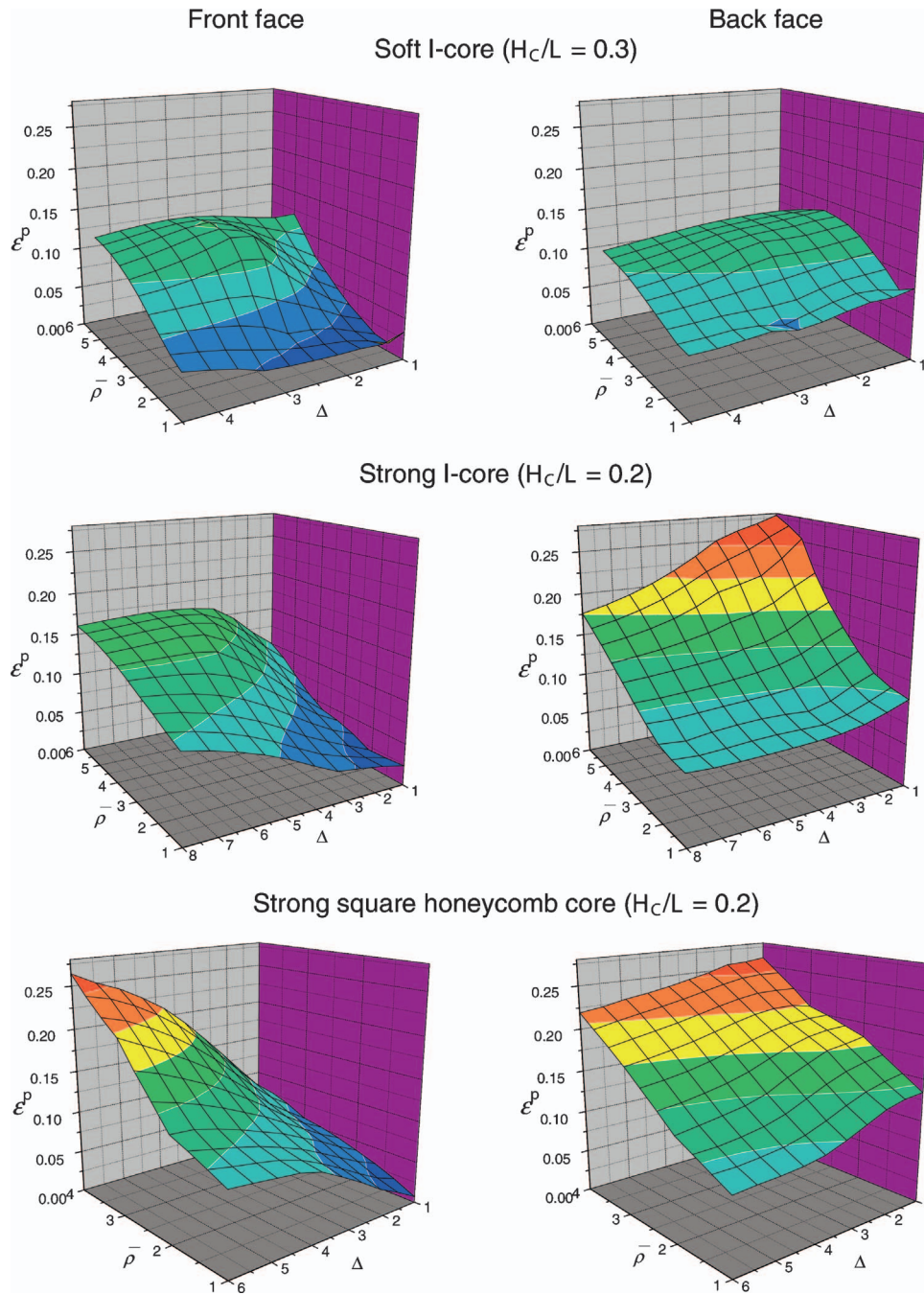
Fig. 14 A synopsis of trends in the maximum plastic strain in the front and back faces, ascertained for a range of strong and soft cores. The coordinates are the ratio of back to front face thickness, Δ, and the relative density of the cores, $\bar{\rho}$.

Initially, the momentum M_T is compared with I_T determined from (11a). It is apparent (Fig. 17) that the analytic formula substantially underestimates the momentum. The magnitude of the underestimate becomes most pronounced for designs with thin front faces and for cores with lower dynamic strength. *The discrepancy suggests that the water imposes a larger momentum than assumed by the existing model.*

Kinetic Energies. Trends in the kinetic energy KE_{II} acquired at the end of stage II with attached water included are plotted in Fig. 18 for a range of STC designs. Comparison with the analytic predictions again reveals that the model substantially underestimates the numerical results.

Transition. The time scales associated with all of the foregoing

results have been used to present a plot of the proposed transition parameter, Π (see Eq. (17)), as a function of core relative density $\bar{\rho}$ and ratio of back to front face thickness Δ (Fig. 19). Overlaying the soft and strong core responses indicates that most of the results can be distinguished by a critical value, $\Pi_{th} \approx 0.2$. That is, smaller values of Π result in strong responses and *vice versa*. However, there are discrepancies, and it remains to establish a rigorous criterion for distinguishing soft and strong responses.

In summary, STC designs can be distinguished by the following characteristics.

    a.   The KE of the two faces and the core all approach zero at time after impact, $t \approx t_{III}$.
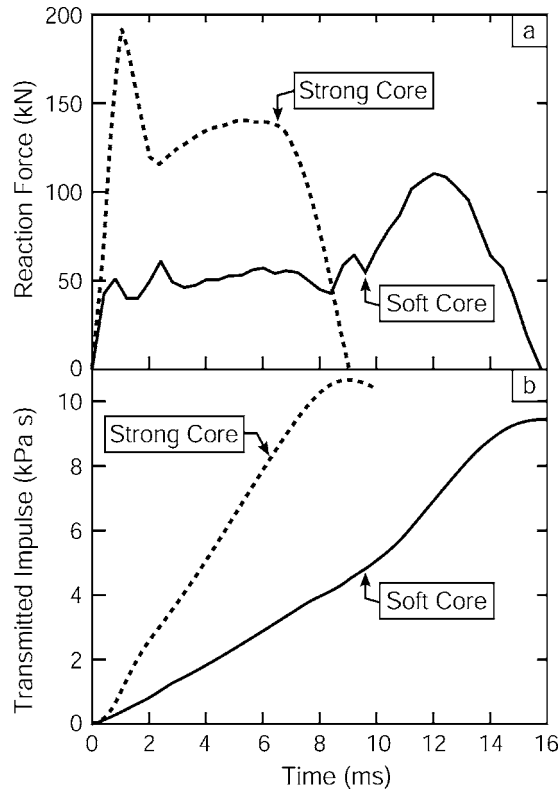
Fig. 15 (*a*) **The reaction forces at the supports typifying the difference between strong and soft cores (results for I-cores are shown).** (*b*) **The corresponding values of the impulse transmitted to the structure determined from the reaction forces.**

b. The front and back faces attain a common velocity at time, $t \approx t_{II}$.

The corresponding SOC characteristics are as follows.

a. The front face and the core retain appreciable KE at times after impact, $t > t_{III}$.
b. The acceleration of the faces stops at time after impact, $t \approx t_b < t_{II}$.
c. Between $t_b < t < t_{II}$, the front face accelerates.

The analytic model consistently underpredicts the acquired momentum and kinetic energy, attributed to an underestimate of the water attached to the wet face at the end of stage II. An alternative FSI model that rectifies this discrepancy for STC designs is presented in the next section. *The remainder of the article is confined to issues affecting the responses of strong core designs.*

7 Alternative Fluid/Structure Interaction Model

7.1 The New Hypothesis. An examination of the velocities and pressures in the water (Fig. 2) indicates that, beyond stage I, a zone of cavitated water exists that widens rapidly with time. Consequently, during stage II, the structure is in contact with cavitated water moving in the same direction. The modified Taylor solution (Eqs. (2) and (3)) does not characterize the response of this zone. An alternative model is needed. The salient features are as follows. Once formed, the left boundary of the cavitation zone (at $x = x_{cb}$) acquires an initial rate of translation, $v_{cb} \approx 10c_w$, away from the panel and then slows asymptotically to c_w (Fig. 20). This speed is supersonic [4] but, more importantly, is initially two orders of magnitude larger than the peak velocity acquired by the front face. Consequently, the cavitation zone expands on a time frame much shorter than the panel structural response, t_{III} [3]. In

addition, the rightmost boundary of the cavitation zone moves quickly towards the panel. Inside the cavitation zone, the pressure is zero, yet the cavitated fluid has *positive velocity* everywhere, causing it to move toward the panel at velocity $v_r(x)$ (Fig. 21). That is, during stage II, a point in the cavitated fluid, initially at x, retains a fixed positive velocity v_r. At locations in the fluid close to the face, v_r exceeds the velocity of the panel, which is decelerating. Such regions within the cavitated fluid (visualized as a porous medium [4]) may thus reattach to the panel, adding momentum. As this happens, these fluid regions decelerate to a velocity approximately equal to the rate of translation of the face at the instant of reattachment. The subsequent fluid pressure in this reattached layer is positive: however, the level oscillates (Fig. 2) due to acoustic interactions with the face and the ongoing reattachment of water. A model incorporating these effects, but eliding some of the complications, will be examined in the following section. The hypothesis is that *any regions within the cavitated fluid having velocity exceeding the ultimate common speed of the structure (attained at the end of stage II) will reattach by the end of that stage and impart additional momentum.*

This hypothesis enables the following three-step analysis.

Step I. Find the location of the cavitation front, x_{cb}, from (2a) by imposing $p = 0$.

Step II. Determine the velocity of the water at the cavitation front $v_{cb}(x_{cb})$ by inserting x_{cb} into (3a). This velocity is found to be insensitive to the time during stage II.

Step III. Assert that this is the velocity of the cavitated water, $v_r(x)$, relative to its location x prior to the arrival of the incoming blast wave.

7.2 Velocity of Cavitated Water. The development is pursued by evaluating the instant, $t_{cb}(x) \geq t_c$, at which cavitation occurs at location x in the water, by solving (2a) at zero pressure:

$$p(x, t_{cb}) = p_0 \left[\exp\left(\frac{x - c_w t_{cb}}{c_w t_o}\right) - \left(\frac{2\beta}{1 - \beta} + \frac{\sigma_{YD}^c}{p_0}\right) \right. $$
$$\times \exp\left(-\frac{\beta(x + c_w t_{cb})}{c_w t_o}\right)$$
$$\left. + \frac{1 + \beta}{1 - \beta} \exp\left(-\frac{x + c_w t_{cb}}{c_w t_o}\right) + \frac{\sigma_{YD}^c}{p_0} \right] = 0 \qquad (22)$$

The ensuing time histories of the location of the cavitation front at time t_{cb} and its rate of translation ($v_{cb} = |dx_{cb}/dt|$) are plotted in Fig. 20. Note that v_{cb} is large, consistent with the preceding discussion. The fluid velocity $v_r(x)$ at the cavitation boundary at the instant of cavitation is now obtained by inserting $t = t_{cb}$ into Eq. (3a):

$$v_r(x) = v(x, t_{cb}) = \frac{2p_o}{\rho_w c_w} \exp\left(\frac{x - c_w t_{cb}(x)}{c_w t_o}\right). \qquad (23)$$

The velocity, $v_r(x)$, obtained in this manner refers to the position, x, of the fluid in its undistorted configuration (in which the density is ρ_w). Since the pressure and pressure gradient in the cavitated zone are zero for $t \geq t_{cb}$ (at least until possible reattachment to the panel), the fluid velocity, $v_r(x)$, remains constant at times $t_c \leq t \leq t_{II}$. It, therefore, represents the actual residual velocity of the water in the cavitation zone. This time invariant velocity profile, $v_r(x)$, is plotted in Fig. 21. Observe the relatively high velocity of the fluid near the sandwich panel.

7.3 The Momentum Transfer. The momentum transferred to the system at the end of stage II becomes:

$$M_T = (m_f + m_c + m_b - \rho_w x_a)v_c. \qquad (24)$$

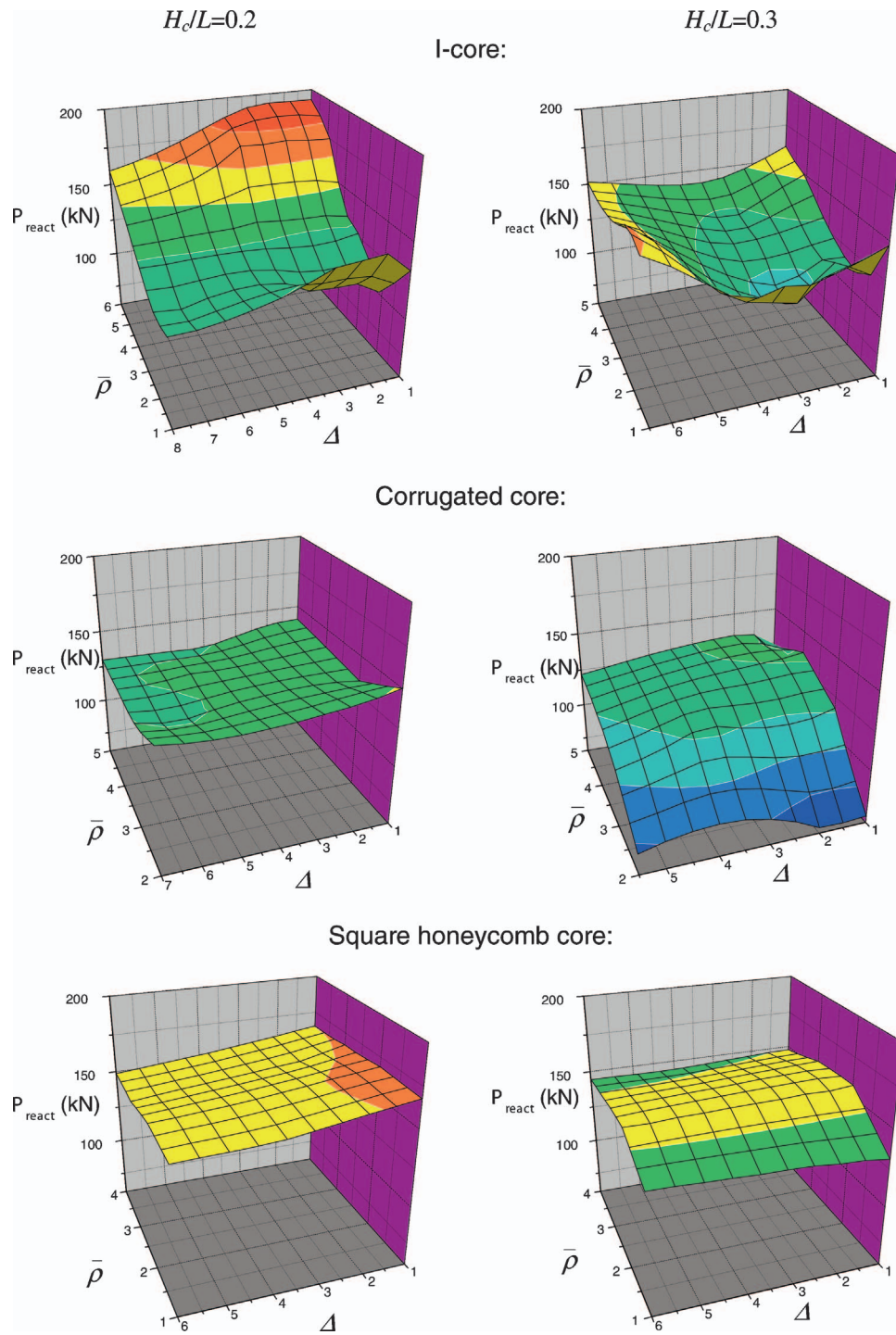The equivalent momentum for the panel plus the same mass of water is:

Fig. 16 A synopsis of trends in the peak reaction force with relative density and ratio of back to front face thickness

$$M_T = \rho_w \int_{x_a}^{x_c} v_r(x) dx + M_F + M_B. \qquad (25)$$

Equating (24) and (25) gives

$$v_c = \frac{\rho_w \int_{x_a}^{x_c} v_r(x) dx + M_F + M_B}{m_f + m_c + m_b - \rho_w x_a}. \qquad (26)$$

Combining (26) with the velocity requirement, $v_r(x_a) = v_c$, gives an equation

$$(m_f + m_c + m_b - \rho_w x_a) v_r(x_a) - \rho_w \int_{x_a}^{x_c} v_r(x) dx = M_F + M_B \qquad (27)$$

that can be solved numerically to obtain x_a and thus v_c. Approximate analytic formulas are given in Appendix B.

The fidelity of this model is tested by comparing the velocity distribution predicted by the improved model with that given by a finite element calculation for a freestanding foam core sandwich panel. The results are presented in Fig. 22. The excellent consis-
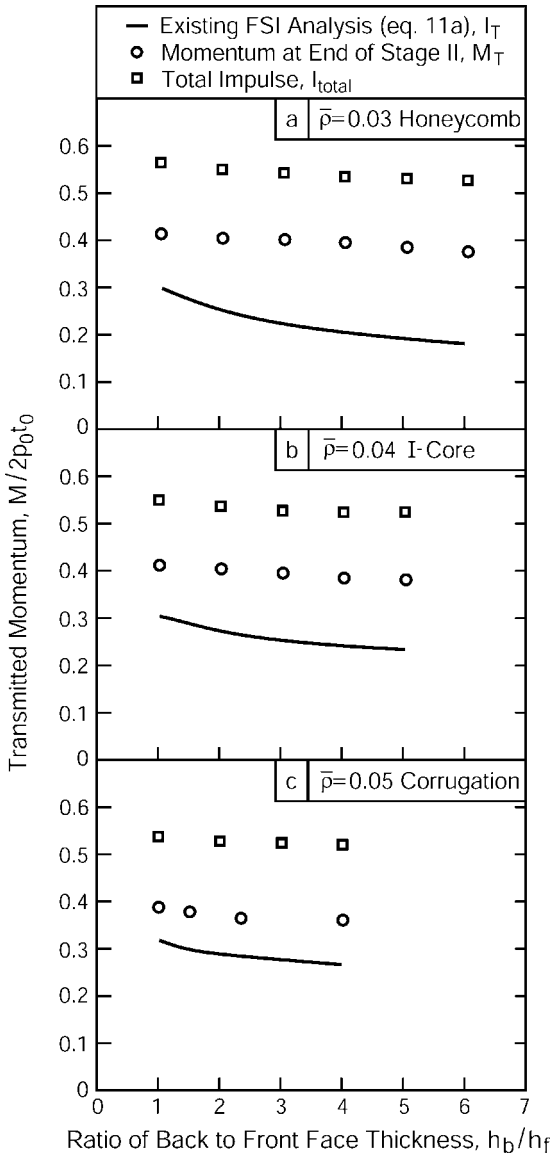
Fig. 17 Trends in the momentum acquired at the end of stage II (structure plus attached water), designated M_T, with ratio of back to front face thickness for a range of strong cores. The total impulse I_{total} transmitted to the system is also plotted. Comparisons with the predicted I_T from the existing analytic model, Eq. (11a), are included.
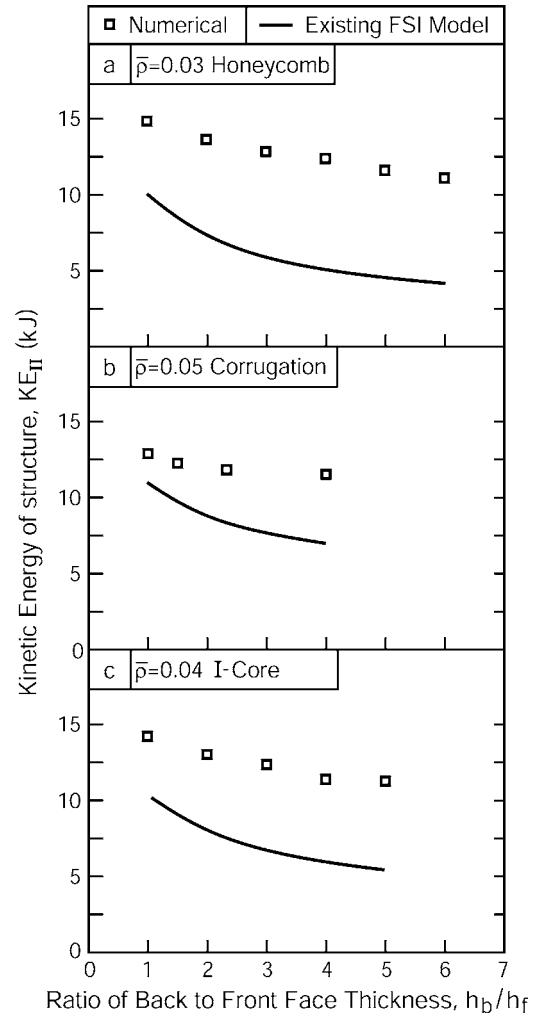

Fig. 18 Trends in the kinetic energies acquired at the end of stage II with ratio of back to front face thickness for a range of strong cores. Results for KE_{II} (structure plus attached water) are plotted. A comparison with the existing analytic model (Eq. (12b)) is included.

tency between the velocity profiles from the model and the simulations justifies the postulate about the common velocity and the extent of reattached water. Another validation is provided by a comparison with numerical results for panels with *foam cores* and steel front and back faces (Fig. 23) [4]. The momentum has been calculated for a freestanding sandwich panel in which the core yield strength parameter, σ_{YD}^c/p_0, was varied from 10^{-3} to 0.5 [4], embracing domains II and III. Inspection of Fig. 23 reveals excellent agreement between the improved model and the finite element simulations.

7.4 Reinterpretation of the Acquired Momentum. Based on this new interpretation of the momentum transfer, the transmitted impulse and the kinetic energy have been recomputed and compared with the present numerical results for strong cores in Figs. 24 and 25. The evident consistency between the numerical and analytic results *affirms the applicability of hypothesis to structured cores*. Note that the total momentum, inclusive of that in the

water (Fig. 24), is appreciably larger than that in the structure and has a different dependence on geometry. Moreover, additional momentum is transferred after the end of stage II, accounting for the difference between the total transmitted impulse (ascertained from the reaction forces) and M_T, evident in the Fig. 17. It will be apparent in the following section that *the deformation of the structure in stage III is controlled by M_{Total} and not the total impulse*. The results also reveal that the benefit of the thin front face in terms of the deflection metric (Fig. 13) is not attributable to its influence on momentum transfer [2,3], but, rather, to the reduced deformations that occur in stage III because of the thick back face [13].

The momentum acquired by the corrugated core compares least favorably with the model, in the sense that the model overpredicts the momentum by ~15%. This discrepancy appears to be linked to the difference in t_{II} between this core and the others (Fig. 11) for reasons yet to be understood. Discrepancies remain for the SOC designs, which do not attain a common velocity. A model capable of predicting the momentum transfer for such cores remains to be developed.

Now that a viable model has been devised for the impulse transmitted to a strong core structure through stage II, the model can be used as input for evaluation of the stage III response, described in the next section.
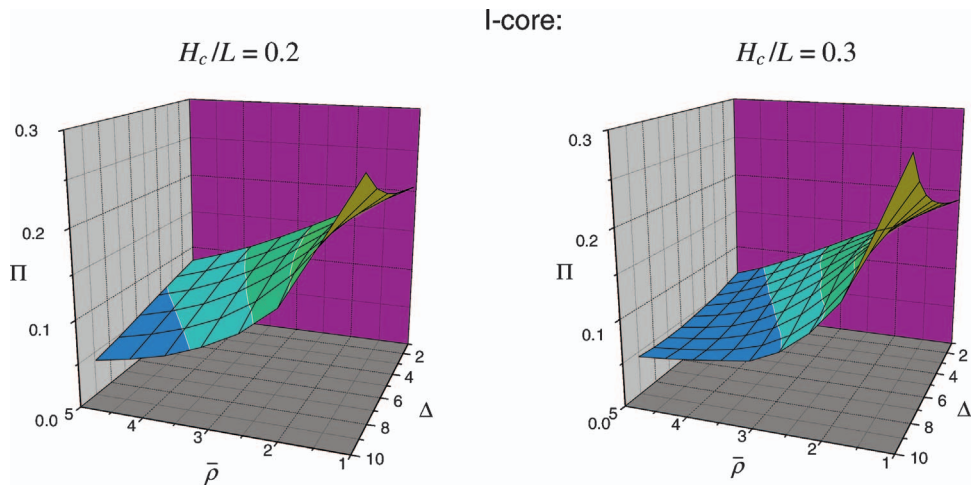
I-core:

$H_c/L = 0.2$

$H_c/L = 0.3$

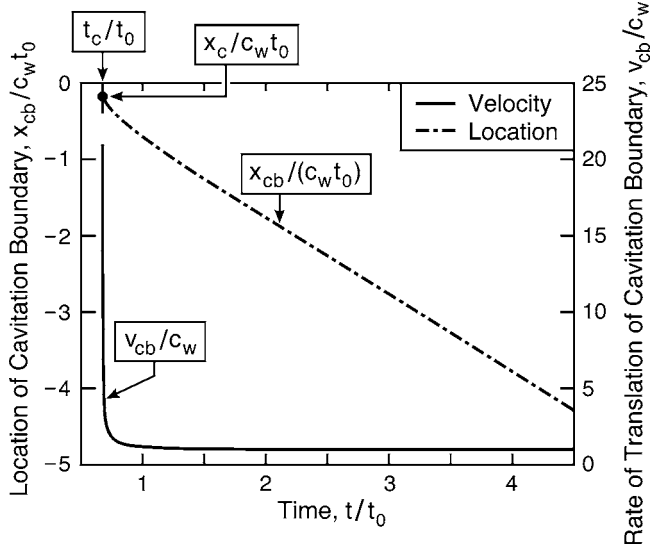**Fig. 19 Trends of the transition parameter Π for I-core design**

Fig. 20 Location and rate of translation of the cavitation boundary as a function of time for the case shown in Fig. 2
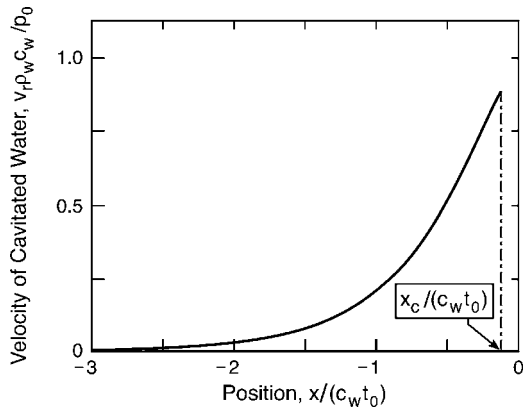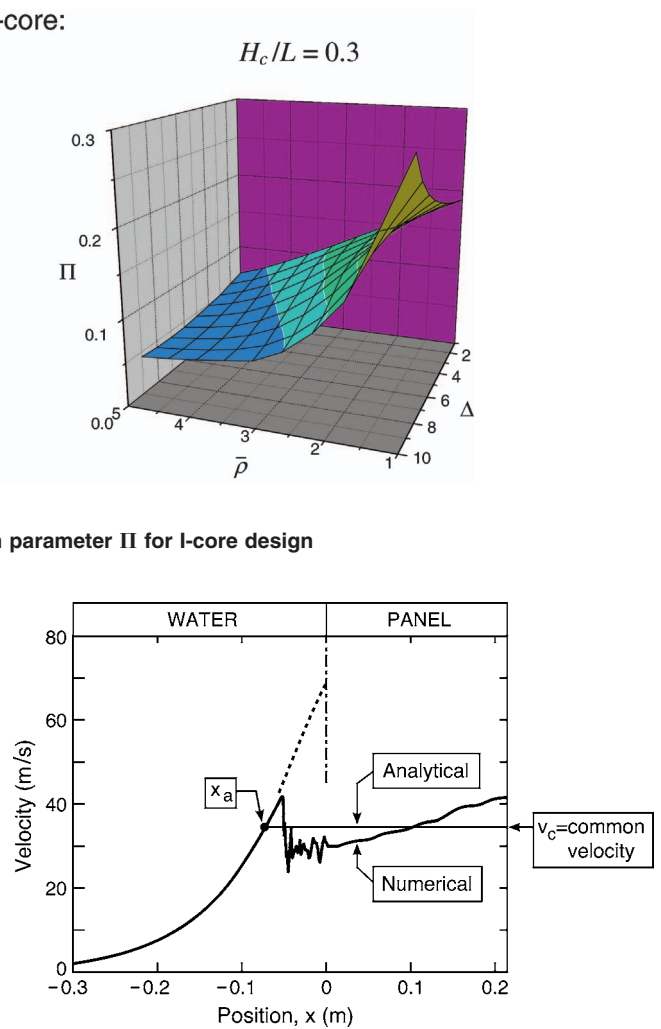

Fig. 22 The velocity distributions at the end of stage II for a foam-core panel ascertained from the new analytic model compared with the result obtained using ABAQUS/Explicit. The core has relative density of $\bar{\rho}_c=0.03$, strength of $\sigma_{YD}^c/p_0=0.18$, and height of $H_c=0.2$ m. The thickness of the front face is $h_f=6$ mm so that $\beta=3.125$ and that of the back face is $h_b=8$ mm.

Fig. 21 Characteristic velocity of cavitated fluid for the case shown in Fig. 2
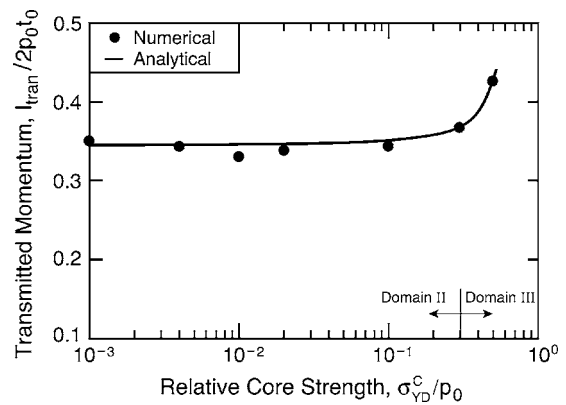

Fig. 23 Comparisons of transmitted momentum calculated using the present model and that obtained numerically by Deshpande and Fleck [4]. The freestanding panel unit has face thickness $h_f=h_b=10$ mm so that $\beta=1.875$, core height $H_c=0.1$ m, the density of the parent metal is 8000 kg/m³, and the relative density of the core is $\bar{\rho}_c=0.1$.
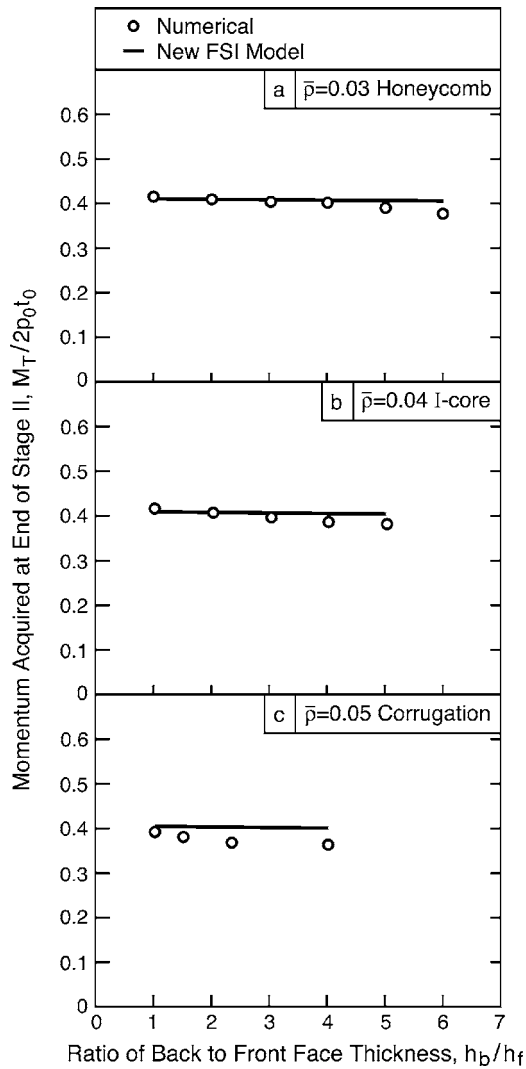
Fig. 24 The momentum at the end of stage II (structure plus attached water) determined numerically and the comparison with the new analytic model (using Eq. (24))
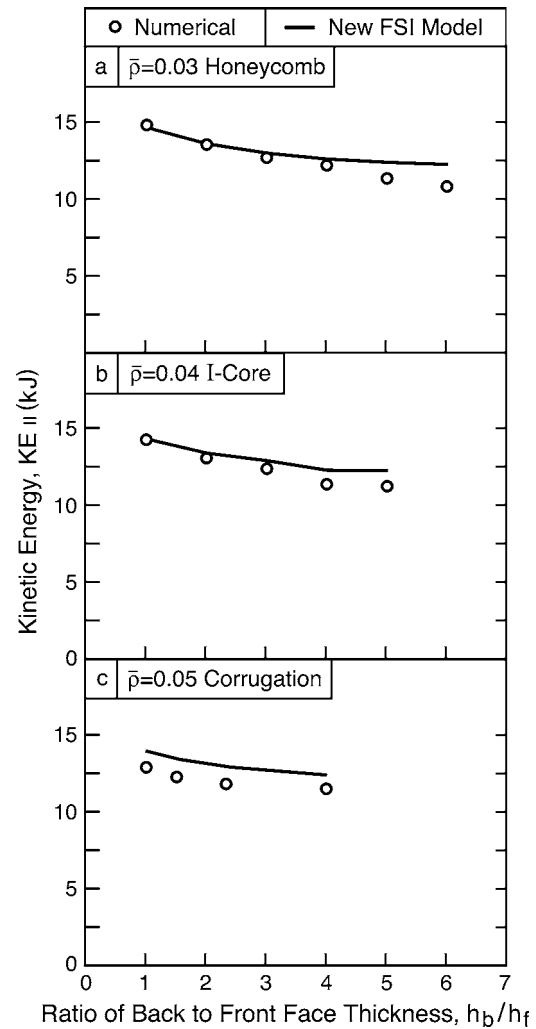

Fig. 25 The kinetic energy at the end of stage II (structure plus attached water) determined with the new analytic model and comparison with numerical calculations for STC design

8 Deflections

The first step in the analysis of the deflections is to ascertain whether KE_{II} (determined using the new model) governs the plastic dissipation, W_{pl}, occurring in stage III, that is, whether the extra momentum transferred during stage III can be discounted. With this objective, plots of the trends in KE_{II} and in the total plastic dissipation, W_{pl}^{total} with panel design (Fig. 26) demonstrate that, when KE_{II} includes the correct contribution from the water, it slightly exceeds W_{pl}^{total}. The slight excess is consistent with a small contribution to stage III dissipation from the elastic reverberations shown on Figs. 9 and 10. *The major implication is that the momentum transferred after the end of stage II does not contribute to the deformation of the panel.* This momentum is transmitted directly to the supports and induces only elastic reverberations in the panel. This finding, in conjunction with the new FSI model, provides a firm basis for predicting the deflections and deformations that occur in stage III, discussed next.

A comparison of the deflections determined numerically with those predicted by (16) has revealed major discrepancies [13]. A deviation is not surprising, given that the deformation modes for the present supports (condition II) differ from the condition I supports used to derive (16). For condition II, most of the deforma-
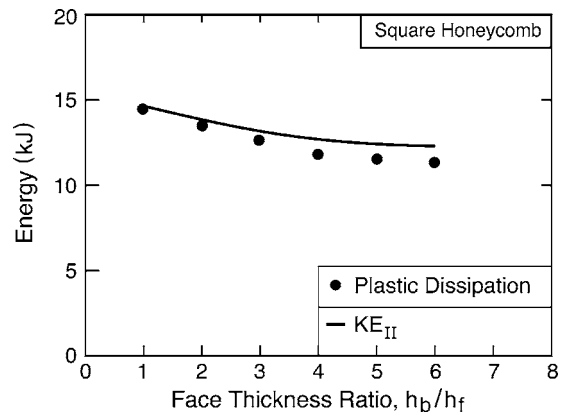

Fig. 26 Comparison of KE_{II} determined using the new analytic model with the total plastic dissipation in stage III calculated numerically. The height of the core is $H_c=0.2L$ and the relative density of the core is $\bar{\rho}=0.03$.

tion occurs through indentation of the back face and the core by the supports (Fig. 8). The sources of the discrepancy and alternative stage III models are discussed elsewhere [13].

9   Concluding Comments

The present assessment has addressed aspects of the response of metallic sandwich structures to underwater blast, emphasizing a domain wherein the water cavitates before the core crushes. It has unearthed several issues affecting the design of high performance panels.

i.   Two regimes have been illustrated exhibiting different trends in displacement, plastic strain and reaction force. One regime, designated STC, has characteristics consistent with an analytic three-stage response model, albeit with quantitative discrepancies. The other, designated SOC, appears to exhibit the best performance. The present results predict that I- and corrugated cores having low relative density, incorporating back faces somewhat thicker than the front, are preferred.

ii.   The behavior of STC designs has been compared with the predictions of a three-stage analytic model [5], which correctly describes the participating events, but has deficiencies. Foremost among these is an underestimate of the momentum imparted to the system by the end of the second stage, attributed to the previously overlooked characteristics of the cavitated water formed by the reflected pressure wave. A new model that accounts fully for the momentum imparted by the end of stage II rectifies the deficiency and accurately predicts the kinetic energy acquired by the structure and attached water. The caviat is that the model only applies to STC designs: characterized by the occurrence of a common velocity for all constituents at the end of stage II. Soft cores do not acquire a common velocity and it remains to extend the present postulate in such a manner that it encompasses these designs.

iii.   For STC designs, the kinetic energy acquired by the end of the second stage accounts fully for the plastic dissipation that occurs in stage III (by bending, stretching, shearing, and indentation of the panel). That is, the extra momentum imparted by the water during this stage does not contribute to the panel deformation. This finding enables the analytically derived kinetic energy at the end of stage II to be used to predict the stage III response. In practice, this opportunity has yet to be realized because the deformation modes differ from those assumed in prior analytical models. Alternative models that rectify this deficiency are explored elsewhere [13].

iv.   Panels supported only at the back face develop smaller front face strains than those supported at both front and back faces, rendering this support system less susceptible to front face tearing. The strains in the back face are larger than those at the front, especially at the supports. The strains in both front and back faces are lowest when SOC designs are used, with implications for designing cores giving the best tearing resistance.

One nuance concerning the momentum transfer merits additional comment. As noted here and elsewhere [2–5], the classical Taylor [17] model is entirely satisfactory for solid plates because cavitation initiates at the plate wet surface, the (constant) velocity acquired by the plate at first cavitation exceeds that for the cavitated water, and there is no layer of attached water on the plate. Thus the momentum and kinetic energy solely in the plate upon first cavitation define the subsequent plastic deformation. The situation differs for the wet face of a sandwich panel *even if the core has negligible strength*. In this case, after acquiring its velocity upon initial cavitation, the front face decelerates, because it compresses the core (which still has mass) and accelerates the back face. Now the cavitated water can catch the decelerating front

face. Consequently, the classical Taylor model [17] underestimates the mass of water by neglecting the reattachment process that occurs during stage II.

Finally we note that the present results for strong cores differ from those presented by Rabczuk et al. [7], who found the lowest center displacement for their corrugated core panels at the lowest relative density. Since their corrugated panels and ours should behave similarly through stage II (despite the orientation orthogonality), the difference is tentatively attributed to the plastic dissipation in stage III, governed especially by the differences in core shear and indentation caused by orientation.

Nomenclature

c_{el} = elastic wave speed in base material

c_w = sound speed in water

E, E_T = Young's modulus and plastic tangent modulus of base material

h_f, h_b = thickness of front face and back face, respectively

H_c = height of the core

H_{eq} = equivalent thickness of the sandwich panel

H_w = height of the water column used in the calculations

I_0 = free field momentum, $I_0 = p_0 t_0$

I_T = transmitted momentum (structure plus water) at the end of stage I

I_{total} = total momentum transmitted to supports

$\bar{I}$ = nondimensional impulse, $\bar{I} = 2 I_0 t_0 / (m_f H_c)$

$\mathrm{KE}_{constituent}$ = kinetic energy of a constituent (e.g., front face, core, or back face)

$\mathrm{KE}_I, \mathrm{KE}_{II}$ = total kinetic energy (structure and attached water) at the end of stages I and II, respectively

KE_{II}^* = kinetic energy of the structure (excluding the water) at the end of stage II

l = spacing between core members

l_w = characteristic length of incident pressure pulse in water, $l_w = c_w t_0$

L = half-width of the sandwich beam

M_B, M_F = momentum of the core plus back face, and that of the front face plus attached water at $t = t_c$

M_T = total momentum of the structure and attached water calculated at t_{II}

m_f, m_c, m_b = mass/area of front face, core, and back face

m_w = mass/area of attached water (added mass) at $t = t_c$

$\bar{m}$ = nondimensional mass, $\bar{m} = m_c / m_f$

p = fluid pressure

p_0 = peak pressure of free field impulse

p' = fluid pressure at $t = t_c$

P_{react} = total reaction force at support

t_0 = characteristic time of incident pressure pulse

$t_I = t_c, t_{II}, t_{III}$ = durations of stages I, II, and III, respectively

t_{arrest} = time at which all constituents are arrested in cases with soft cores

t_b = time at which the back face acceleration stops

t_{cb} = time at which the cavitation boundary arrives at location $x = x_{cb}$

v = fluid velocity used in the extended Taylor model
v' = fluid velocity at $t=t_c$
v_b, v_f = average velocities of back face and front face, respectively
v_c = common velocity of structure and attached water in the new FSI model
v_{cb} = rate of translation of the cavitation boundary
v_{common} = common average velocity of all constituents at the end of stage II
v_{face} = velocity of front face at $t=t_c$
v_r = residual velocity of cavitated water used in the new FSI model
$W_{pl}^{constituent}$ = plastic dissipation in a constituent
W_{pl}^{total} = total plastic dissipation in the beam during stage III
x = distance from front face of the panel, with water residing in $x<0$
x_a = width of the attached water from the new FSI model at the end of stage II
x_c = location of first cavitation in water
x_{cb} = location of the cavitation boundary
β = fluid-structure interaction parameter, $\beta = \rho_w c_w t_0 / m_f$
δ_f, δ_b = mid-span deflection of front and back face, respectively
Δ = ratio of face plate thickness, $\Delta = h_b / h_f$
ε_c = core crush strain
ε_{pl}^{max} = maximum plastic strain in face plates
ε_Y = yield strain of base material
ζ, ξ = dimensionless parameters used for wave propagation in Sec. 2
$\bar{\rho}$ = relative density of the core
ρ, ρ_w = density of base metal and that of water, respectively
σ_Y = yield strength of base material
σ_{YD}^c = dynamic yield strength of the core.

Appendix A: A Synopsis of Numerical Simulations for Square Panels

The numerical model described in Sec. 5 has been used to simulate square panels for each of the core topologies. For the simulations, the panels are supported along the entire perimeter around the back face. An example of a simulation for a strong I-core, relative to that for a beam, is presented in Fig. 27: the deformed shapes at the bottom (beam) and top (panel) have been obtained using separate simulations. Note that the central areas of the plates experience about the same deflections as the mid-span areas of the beams. Moreover, the buckling modes of the core members are identical. This result is typical of many such comparative simulations.

Appendix B: Analytic Approximations

Many numerical simulations have been carried out for a wide parameter range ($0 < \sigma_{YD}^c / p_0 < 0.35$ and $0 < \beta < 8$) encompassing domain II. The results have been fitted into analytical forms that can be used with Eqs. (24) and (25) to determine the final momentum for any sandwich design within this domain. The first cavitation plane is located at

$$\bar{x}_c \equiv \frac{x_c}{c_w t_0} \approx 4.8 \left(\frac{\sigma_{YD}^c}{p_0} \right)^{1.1} (0.24 - 0.015\beta + 0.0012\beta^2). \quad (B1)$$

An exponential function is most applicable for the reference field:

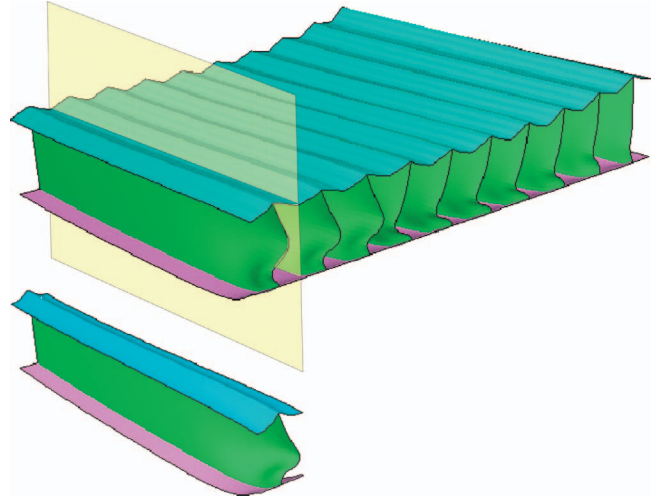$$\bar{v}_r \equiv \frac{v_r}{p_0/(\rho_w c_w)} = A \exp(\bar{x}/T), \quad (B2)$$

with

Fig. 27 Deformed shape of the square I-core plate (top picture, $\frac{1}{4}$ of the plate shown) and the I-core beam (bottom picture, $\frac{1}{2}$ of the beam shown)

$$A \approx (0.08 + 2.2\beta)f(\beta)\left[1 - 0.28\frac{\sigma_{YD}^c}{p_0} - 0.18\left(\frac{\sigma_{YD}^c}{p_0} \right)^2 \right],$$

$$T \approx (0.63 - 0.028\beta + 0.003\beta^2)\left(1 - 0.047\frac{\sigma_{YD}^c}{p_0} \right),$$

where $f(\beta) = \beta^{\beta/(1-\beta)}$. Since, at location $\bar{x} = \bar{x}_a$, $\bar{v}_c = \bar{v}_r(\bar{x}_a)$, therefore

$$\bar{x}_a = T(\ln \bar{v}_c - \ln A) \quad (B3)$$

With Eqs. (B1) to (B3), Eq. (26) can be rewritten as

$$\bar{v}_c = \frac{I_T + A \cdot T \cdot \exp(\bar{x}_c/T)}{\dfrac{m_f + m_c + m_b}{\rho_w c_w t_0} - T(\ln \bar{v}_c - \ln A - 1)}, \quad (B4)$$

which can be solved for $\bar{v}_c$ and thus $\bar{x}_a$.

References

[1] Xue, Z., and Hutchinson, J. W., 2003, "Preliminary Assessment of Sandwich Plates Subject to Blast Loads," Int. J. Mech. Sci., **45**, pp. 687–705.
[2] Xue, Z., and Hutchinson, J. W., 2004, "A Comparative Study of Impulse-Resistant Metallic Sandwich Plates," Int. J. Impact Eng., **30**, pp. 1283–1305.
[3] Fleck, N. A., and Deshpande, V. S., 2004, "The Resistance of Clamped Sandwich Beams to Shock Loading," ASME J. Appl. Mech., **71**, pp. 386–401.
[4] Deshpande, V. S., and Fleck, N. A., 2005, "One-Dimensional Shock Response of Sandwich Plates," J. Mech. Phys. Solids, **53**, pp. 2347–2383.
[5] Hutchinson, J. W., and Xue, Z., 2005, "Metal Sandwich Plates Optimized for Pressure Impulses," Int. J. Mech. Sci., **47**, pp. 545–569.
[6] Qiu, X., Deshpande, V. S., and Fleck, N. A., 2003, "Finite Element Analysis of the Dynamic Response of Clamped Sandwich Beams Subject to Shock Loading," Eur. J. Mech. A/Solids, **22**, pp. 801–814.
[7] Rabczuk, T., Samaniego, E., and Belytschko, T., 2005, "Simplified Model for Predicting Impulse Loads on Submerged Structures to Account for Fluid-Structure Interaction," Int. J. Impact Engng., in press.
[8] Xue, Z., and Hutchinson, J. W., 2005, "Crush Dynamics of Square Honeycomb Sandwich Cores," Int. J. Numer. Methods Eng., **65**, pp. 2221–2245.

[9] Cole, R. H., 1948, *Underwater Explosions*, Princeton University Press, Princeton, NJ.

[10] Hunter, K. S., and Geers, T. L., 2004, "Pressure and Velocity Fields Produced by an Underwater Explosion," J. Acoust. Soc. Am., **115**, pp. 1483–1496.

[11] Shin, Y. S., 2004, "Ship Shock Modeling and Simulation for Far-Field Underwater Explosion," Comput. Struct., **82**, pp. 2211–2219.

[12] Klaseboer, E., Hung, K. C., Wang, C., Wang, C. W., Khoo, B. C., Boyce, P., Debono, S., and Charlier, H., 2005, "Experimental and Numerical Investigation of the Dynamics of an Underwater Explosion Bubble Near a Resilient/ Rigid Structure," J. Fluid Mech., **537**, pp. 387–413.

[13] Hayhurst, D. R., Flores, S., McMeeking, R. M., and Evans, A. G., 2005, "The Response of Metallic Panels to Water Blast: Deflections," submitted for publication.

[14] Deshpande, V. S., and Fleck, N. A., 2005, private communication.

[15] Ashby, M. F., Evans, A. G., Fleck, N. A., Gibson, L. J., Hutchinson, J. W., and Wadley, H. N. G., 2000, *Metal Foams: A Design Guide*, Butterworth-Heinemann, Boston.

[16] ABAQUS/Explicit User's Manual, Version 6.4. Hibbitt, Karlsson and Sorensen Inc., 2003.

[17] Taylor, G. I., 1963, "The Pressure and Impulse of Submarine Explosion Waves on Plates," in *The Scientific Papers of G.I. Taylor*, Vol. III, Cambridge University Press, Cambridge, UK, pp. 287–303.